

Terrestrial analogues for lunar impact melt flows



C.D. Neish^{a,b,*}, C.W. Hamilton^c, S.S. Hughes^d, S. Kobs Nawotniak^d, W.B. Garry^e, J.R. Skok^f, R.C. Elphic^g, E. Schaefer^c, L.M. Carter^e, J.L. Bandfield^h, G.R. Osinski^{a,b}, D. Lim^{g,i}, J.L. Heldmann^g

^a Department of Earth Sciences, The University of Western Ontario, London, ON, N6A 5B7

^b Centre for Planetary Science and Exploration, The University of Western Ontario, London, ON, N6A 5B7

^c Lunar and Planetary Laboratory, University of Arizona, Tucson, AZ, 85721

^d Idaho State University, Pocatello, ID, 83209

^e NASA Goddard Space Flight Center, Greenbelt, MD, 20771

^f SETI Institute, Mountain View, CA, 94043

^g NASA Ames Research Center, Mountain View, CA, 94035

^h Space Science Institute, Boulder, CO, 80301

ⁱ Bay Area Environmental Research Institute, Petaluma, CA, 94952

ARTICLE INFO

Article history:

Received 29 February 2016

Revised 4 August 2016

Accepted 5 August 2016

Available online 6 August 2016

Keywords:

Earth

Impact processes

Moon, surface

Radar observations

Volcanism

ABSTRACT

Lunar impact melt deposits have unique physical properties. They have among the highest observed radar returns at S-Band (12.6 cm wavelength), implying that they are rough at the decimeter scale. However, they are also observed in high-resolution optical imagery to be quite smooth at the meter scale. These characteristics distinguish them from well-studied terrestrial analogues, such as Hawaiian pāhoehoe and ‘a‘ā lava flows. The morphology of impact melt deposits can be related to their emplacement conditions, so understanding the origin of these unique surface properties will help to inform us as to the circumstances under which they were formed. In this work, we seek to find a terrestrial analogue for well-preserved lunar impact melt flows by examining fresh lava flows on Earth. We compare the radar return and high-resolution topographic variations of impact melt flows to terrestrial lava flows with a range of surface textures. The lava flows examined in this work range from smooth Hawaiian pāhoehoe to transitional basaltic flows at Craters of the Moon (COTM) National Monument and Preserve in Idaho to rubbly and spiny pāhoehoe-like flows at the recent eruption at Holuhraun in Iceland. The physical properties of lunar impact melt flows appear to differ from those of all the terrestrial lava flows studied in this work. This may be due to (a) differences in post-emplacement modification processes or (b) fundamental differences in the surface texture of the melt flows due to the melts' unique emplacement and/or cooling environment. Information about the surface properties of lunar impact melt deposits will be critical for future landed missions that wish to sample these materials.

© 2016 Elsevier Inc. All rights reserved.

1. Introduction

The formation of melt is a fundamental part of the impact cratering process. The high shock pressures experienced during impact causes the target rock to melt, forming a layer that lines the transient cavity (Melosh, 1989). Much of this material remains within the final crater, but some impact melt may be ejected from the crater or draped over the rim. Indeed, deposits of melted material are often observed exterior to fresh impact craters on terrestrial planets (e.g., Howard and Wilshire, 1975; Hawke and Head, 1977). These deposits have differing volumes and morphologies,

which vary with crater diameter (Cintala and Grieve, 1988). Coherent flows of melt are observed exterior to many craters on the Moon, over a large range of diameters (Carter et al., 2012; Denevi et al., 2012; Stopar et al., 2014; Neish et al., 2014). In some cases, there is evidence for a complex post-emplacement history, including multi-stage influx of melt into flow lobes (Bray et al., 2010). The extent of melt movement has implications for the physical properties of the melt, surface topography, and the timing of modification in complex craters (e.g., Osinski et al., 2011). Thus, studying the properties of these deposits will lead to a deeper understanding of this important geologic process.

Lunar impact melt deposits have unique physical properties compared to other lunar materials. Impact melt deposits have among the highest observed radar returns on the surface of the

* Corresponding author.

E-mail address: cneish@uwo.ca (C.D. Neish).

Moon (Campbell et al., 2010; Carter et al., 2012; Neish et al., 2014). They commonly have S-Band (12.6 cm wavelength) circular polarization ratios near or exceeding one, a result consistent with scattering from decimeter scale rock edges, cracks, or natural corner reflectors (Campbell, 2012). The only other materials on the Moon with similar radar properties are ejecta blankets around fresh craters, which are composed of rocks and boulders of differing sizes, found at the surface and within a fine-grained regolith matrix (Campbell, 2012). However, when viewed in high-resolution optical imagery, the lunar impact melt flows appear smooth at the meter scale (Bray et al., 2010; Neish et al., 2014; Stopar et al., 2014), unlike ejecta blankets, which remain ‘rough’ at these scales (Ghent et al., 2010; Bandfield et al., 2011).

It may be possible to constrain the physical properties of impact melt flows by comparisons to lava flows on the Earth and other planets. Although they have different origins, impact melt flows and lava flows are both composed of melted rock that flows over a planetary surface under the influence of gravity, cooling and crystallizing in the process. In many cases, the morphologies of impact melt flows appear very similar to the morphologies of terrestrial lava flows, although they also exhibit distinct features such as erosional channels (Bray et al., 2010; Denevi et al., 2012). As with lava flows, the morphology of impact melt flows can be related to their emplacement conditions and melt properties through thermo-rheological models (cf., Gregg and Fink, 2000). For example, initial measurements of the three dimensional structure of lunar impact melts appear most consistent with superheated, low viscosity flows (Denevi et al., 2012). Understanding the origin of their unique surface properties will further inform us as to the conditions at which they were emplaced.

However, the surface characteristics of lunar impact melt flows – rough at decimeter scales and smooth at meter scales – are unlike any terrestrial lava flows yet studied. Terrestrial pāhoehoe flows in Hawai‘i are smooth at both decimeter and meter scales (Campbell and Shepard, 1996), and have low circular polarization ratios (Campbell, 2002). ‘a‘ā flows are rougher at both scales, but have moderate circular polarization ratios that do not exceed one. Blocky, andesitic flows have circular polarization ratios that do exceed one (Campbell et al., 1993), but they are typically rough at meter scales, as measured by their root mean square height and slope (Shepard et al., 2001).

Still, several types of terrestrial lava flows have not been extensively studied at radar wavelengths, and may prove to be better analogues to lunar impact melt deposits than pāhoehoe and ‘a‘ā end-members. In particular, a variety of ‘transitional’ lava flow types may develop if the surface of a pāhoehoe-like flow is disrupted. These flows produce ‘platy’ or ‘slabby’ lava flows consisting of a series of large slabs or ‘rubbly’ lava flows if the slabs are disrupted into smaller pieces (Keszthelyi et al., 2004). Rubble differs significantly from ‘a‘ā clinker in that it is not spinose due to viscous tearing, but instead blocky due to mechanical fragmentation of an already brittle crust (Guilbaud et al., 2005). As such, it likely has different radar scattering properties than ‘a‘ā flows and may present a better analogue to lunar impact melt flows. Indeed, platy lava flows have been identified by Keszthelyi et al. (2004) in the Cerberus Plains on Mars, and many of these flows have high circular polarization ratios (Harmon et al., 2012), similar to lunar impact melt flows.

There are only a few regions on Earth where transitional lava flows have been imaged with synthetic aperture radar. One location is the Craters of the Moon (COTM) lava field in Idaho (Campbell et al., 1989; Khan et al., 2007). COTM is located in Idaho’s Great Rift volcanic zone and is the largest dominantly Holocene basaltic lava field in the contiguous United States, formed over eight major eruptive events during the last 15,000 years (Kuntz et al., 1992). This polygenetic lava field shows a great diver-

sity of volcanic features, including transitional lava types, such as slabby and blocky flows (Hughes et al., 1999). Transitional lava flow textures are also found in Iceland. Keszthelyi et al. (2004) found examples of surfaces composed primarily of disrupted pāhoehoe on lava flows that were hundreds to thousands of years old. More recently, the Holuhraun eruption generated a wide range of surface textures, including spiny pāhoehoe, rubbly and slabby lavas, and ‘a‘ā (Pederson et al., 2015; Hamilton, 2015).

In this work, we seek to identify a terrestrial analogue to lunar impact melt flows, with a particular focus on transitional lava morphologies. We characterize the roughness properties of transitional lava flows for the first time and compare them to similar properties for the more extensively studied Hawaiian lavas. These include both pāhoehoe and ‘a‘ā flows in Kilauea and Mauna Ulu. We determine the root mean square height, root mean square slope, and Hurst exponent of the flows at a range of scales, using high-resolution topographic profiles acquired in the field. We compare these results to L-Band (24 cm wavelength) radar data acquired over the same flows.

Finally, we compare the roughness properties of the lava flows to the properties of impact melt deposits on the Moon. We use images acquired by the S-Band (12.6 cm wavelength) Mini-RF instrument on board the Lunar Reconnaissance Orbiter (LRO) (Nozette et al., 2010), the digital terrain models (DTM) produced from LRO Narrow Angle Camera (NAC) images (Robinson et al., 2010), and surface roughness properties derived from LRO Diviner Radiometer measurements (Paige et al., 2010). In this work, we focus specifically on an impact melt flow emanating from a lunar crater on the rim of Korolev X (located on the lunar farside at 0.56°N, 159.44°W) (Osinski et al., 2011). There are only a handful of DTMs of lunar impact melt flows that are publicly available through the Planetary Data System, and of these, the melt flow at Korolev X is the largest and best preserved example. By examining this representative melt flow, we aim to identify appropriate terrestrial analogues for these unusual materials, to help us understand their emplacement conditions and evolution over time.

2. Surface roughness from topographic data

2.1. Technique

The roughness of a surface is typically defined by its topography over horizontal scales of centimeters to a few hundred meters. However, to compare the relative roughness of different surfaces, we need a standardized way to quantify this value. Shepard et al. (2001) looked at the various methods used to quantify surface roughness, and suggested a standard method for computing relevant parameters. Following their recommendation, in this work we report the root mean square (RMS) height and slope of the surface at a variety of scales, as well as the scaling behavior of the surface roughness as quantified by the Hurst exponent.

The RMS height, h_{rms} , is the standard deviation of heights about the mean (Eq. (1)):

$$h_{rms} = \left[\frac{1}{n-1} \sum_{i=1}^n [z(x_i) - \bar{z}]^2 \right]^{1/2} \quad (1)$$

Here, n is the number of sample points, $z(x_i)$ is the height of the surface at point x_i , and \bar{z} is the mean height of the profile. Typically the profile is detrended by removing the best-fit linear function from the data. In this case, the mean height is zero. The RMS slope can be determined from the Allan variance, v^2 (Eq. (2)):

$$v^2(\Delta x) = \frac{1}{n} \sum_{i=1}^n [z(x_i) - z(x_i + \Delta x)]^2 \quad (2)$$

Here, the topographic profile is sampled at every step Δx , and the RMS difference in heights is calculated. From this, we can calculate the RMS slope, s_{rms} , at a variety of step sizes (Eq. (3)):

$$s_{rms} = \frac{v(\Delta x)}{\Delta x} \quad (3)$$

Both the RMS height and the RMS slope are dependent on the scales over which they are measured. Most natural surfaces can be described by a ‘fractal’ or ‘self-affine’ scaling behavior (Turcotte, 1997), characterized by the Hurst exponent, H (Eqs. (4)–(6)).

$$h_0(L) = C_h \left(\frac{L}{L_0} \right)^H \quad (4)$$

$$v(\Delta x) = C_s \left(\frac{\Delta x}{\Delta x_0} \right)^H \quad (5)$$

$$s_0(\Delta x) = \frac{v(\Delta x)}{(\Delta x/\Delta x_0)} = C_s \left(\frac{\Delta x}{\Delta x_0} \right)^{H-1} \quad (6)$$

Here, L is the length of the profile, Δx is the step size, and C_h and C_s are the RMS height and slope at the reference scales L_0 and Δx_0 . The Hurst exponent ranges from zero to one. A Hurst exponent close to zero indicates that the surface becomes smooth as the scale increases (e.g., a grass lawn). A Hurst exponent close to one indicates that the surface maintains its roughness (or smoothness) as the scale increases. A surface is equally rough (or smooth) at any scale at $H = 1$. A Hurst exponent of 0.5 is termed ‘Brownian’, since Brownian motion will produce a surface of this form. Many natural surfaces tend to cluster about this value (Shepard et al., 2001). In many cases, this scaling behavior only works for a limited range of scales and there is a ‘break point’ in the scaling that disconnects large-scale from fine-scale roughness. In these cases, one must calculate the parameters on each side of the break point (Shepard et al., 2001).

2.2. Topographic data

In this work, we acquired one-dimensional profiles with differential GPS (dGPS) over various lava flow surfaces in three locales: two locations that exhibit ‘transitional’ lava flow textures (COTM and the new lava flow at Holuhraun in Iceland), and one location that exhibits the well-studied pāhoehoe and ‘a’ā end-members (Mauna Ulu). The profiles were typically tens of meters to over one hundred meters long. The horizontal spacing varied from profile to profile but was always less than 25 cm (see Table 1). The only exception was Profile A at COTM, which was conducted in manual rather than continuous collection mode, and produced a spacing of 26 ± 12 cm. The profiles have a vertical accuracy of better than 2 cm and a vertical precision of 6–8 cm (based on the method of Hamilton et al. (2010)). Roughness properties may have directional biases (Morris et al., 2008), so when possible, we collected profiles in perpendicular directions.

The topographic profile from each lava flow was detrended by removing the best-fit linear function from the data. This was done in order to replicate the technique used by Campbell (2002), so that we could compare our results directly. The profiles were then interpolated, and heights extracted at step sizes Δx ranging from 0.25 m to 12 m. The Allan variance was calculated for each step size, and the Hurst exponent and RMS slope (at 1 m reference scale) were determined from linear fits to the variogram. The Hurst exponent is computed from the slope of the fit, and the RMS slope is computed from the y-intercept of the fit (Eq. (7)).

$$\log(v(\Delta x)) = \log(C_s) + H \log(\Delta x) \quad (7)$$

Fits at two different scales were completed – one over the range 0.25 m to 2 m, and one over the range 2 m to 12 m. Ideally, the profile length should be a minimum of 10 times the length

of the largest scale being investigated (Shepard et al., 2001), but we found a better fits to the variogram if we included a 12 m baseline (12% of 100 m) instead of stopping at a 10 m baseline. In the latter case, a 2 m-long low pass filter was applied to aid in comparisons with the lower resolution lunar data. This was accomplished by calculating the moving average of the topographic profile, averaging runs of eight elements spaced 25 cm apart to produce a smoothed 2 m profile. The results of these fits, as well as the standard error of the fits, are reported in Table 1. In addition, the RMS height was calculated for each one-meter section of the profile (with a horizontal spacing of 25 cm), and the average is reported in Table 1.

In COTM, the profiles were collected over five distinct types of lava flows (Figs. 1 and 2). The basalts at COTM have a range of chemical compositions, and tend to have higher silica (SiO_2) content than typical tholeiitic basalts in the surrounding monogenetic lava fields (Hughes et al., 1999, 2004). This produces lava flows with a range of different textures. The ‘billowy’ pāhoehoe is characterized by large lobes of smooth pāhoehoe that typically have elongated gas bubbles on the surface that form spines. The ‘lava pond’ is a ponded section of the pāhoehoe flow. Transitional lava flow types are also present. The ‘slabby’ lava has a surface composed of disrupted plates of broken pāhoehoe crust, which are decimeters to meters in size in the horizontal dimension and centimeters in size in the vertical dimension. The ‘rubbly’ lava is similar to the slabby lava, but the broken pieces of pāhoehoe are roughly the same size in all dimensions. The ‘blocky’ lava has a surface composed of angular blocks, which tend to be several decimeters in dimension. Representative topographic profiles for each of these lava flows are shown in Fig. 3, and example variograms are shown in Fig. 4.

Next, we compared the data collected in COTM to topographic profiles acquired over basaltic lava flows in Hawai‘i. Campbell (2002) report the RMS height, RMS slope, and Hurst exponent for ten profiles acquired on Kīlauea Volcano, for horizontal step sizes between 0.25 m and 2 m. Similar profiles were also obtained over fresh and degraded pāhoehoe lava flows in the distal SE margin of the Mauna Ulu lava flow (Figs. 5 and 6). The Mauna Ulu eruption initiated on 24 May 1969, and lasted until 24 July 1974. Basaltic lava extruded from Mauna Ulu covers 61 km² and includes a wide range of ‘a’ā and pāhoehoe flow types (Swanson et al., 1979; Tilling et al., 1987; Byrnes et al., 2001). Of particular interest within this study is the lava located in the medial to distal portions of the SE flow branch, which is composed of dense, hummocky pāhoehoe that was fed by a network of internal pathways (i.e., lava tubes) that transported lava beneath a stable crust that underwent significant inflation (Peterson and Swanson, 1974; Walker, 1991). This study area is located just to the south of the region investigated by Byrnes et al. (2001). In that region, sheet-like pāhoehoe flows overlie similar pre-historic pāhoehoe lava flows, and both flows exhibit prominent inflation features such as tumuli. It is interesting to note that evidence of broad-scale inflation has also been observed in some lunar impact melt flows, including one at Giordano Bruno (Bray et al., 2010), but localized inflation structures (e.g., tumuli) have not been observed within impact melts to date. Both the modern and prehistoric lava flows were analyzed in the exact same manner as the flows in COTM. The values for RMS height, RMS slope, and Hurst exponent are reported in Table 1.

Finally, we determined the roughness properties for four different regions on the fresh Icelandic lava flow at Holuhraun (Figs. 7 and 8). This eruption began on 31 August 2014 and lasted until 28 February 2015. The erupted lava had an olivine tholeiite composition with a minor abundance of phenocrysts and a ground-mass containing silicate glass with plagioclase, clinopyroxene, and olivine microlites (Gíslason et al., 2015). The eruption generated 1.6 ± 0.3 km³ of magma and produced a lava flow covering 84.1 ± 0.6

Table 1
Roughness properties of lava flows at Craters of the Moon National Monument, the 2014–2015 eruption at Holuhraun in Iceland, Hawai'i Volcanoes National Park, a lunar impact melt, and a lunar lava flow.

Profile	Type of lava	Profile length (m)	Horizontal spacing (cm) ^a	Vertical accuracy (cm)	C _h (1 m) (cm)	C _s ^b (°)	H ^b	C _s ^c (°)	H ^c
COTM – LP	Lava pond	100	16 ± 2	1.5	5.3	7.2 ± 0.2	0.42 ± 0.04	5.1 ± 0.5	0.50 ± 0.05
COTM – Alt	Rubby lava	40	16 ± 2	1.5	13.3	15.1 ± 0.6	0.28 ± 0.06	16 ± 6	0.0 ± 0.2
COTM – A	Slabby lava	100	26 ± 12	2	14.0	16.8 ± 0.4	0.52 ± 0.04	16 ± 2	0.14 ± 0.05
COTM – B	Slabby lava	65	19 ± 8	2	15.8	20.4 ± 0.6	0.50 ± 0.05	16 ± 3	0.3 ± 0.1
COTM – X1	Billowy pāhoehoe	100	15 ± 3	1.5	16.3	22.0 ± 0.7	0.52 ± 0.04	17 ± 3	0.49 ± 0.09
COTM – X2	Billowy pāhoehoe	100	16 ± 3	1.5	15.2	21.1 ± 0.5	0.53 ± 0.04	16 ± 1	0.61 ± 0.04
COTM – K2	Blocky lava	90	16 ± 3	1.5	19.7	24 ± 1	0.45 ± 0.06	18 ± 6	0.3 ± 0.2
COTM – K3	Blocky lava	70	17 ± 3	1.5	16.6	23 ± 1	0.46 ± 0.07	25 ± 7	0.1 ± 0.1
Holuhraun – H2	Spiny pond	40	11 ± 2	1	7.5	10 ± 1	0.2 ± 0.2	5.7 ± 0.6	0.27 ± 0.05
Holuhraun – H4	Spiny pāhoehoe	40	10 ± 3	1	4.4	5.4 ± 0.2	0.24 ± 0.06	4.2 ± 0.5	0.30 ± 0.06
Holuhraun – H5	Slabby lava	40	10 ± 2	1	13.7	16.1 ± 0.5	0.41 ± 0.04	11 ± 3	0.3 ± 0.2
Holuhraun – H7	Rubby lava	40	9 ± 3	1	17.4	16.6 ± 0.5	0.18 ± 0.04	6 ± 2	0.5 ± 0.2
Mauna Ulu – M5	Fresh, smooth pāhoehoe	100	20	2	5.1	8.8 ± 0.2	0.70 ± 0.03	8 ± 1	0.76 ± 0.08
Mauna Ulu – M6	Fresh, smooth pāhoehoe	100	20	2	7.3	13.3 ± 0.1	0.75 ± 0.01	15 ± 3	0.5 ± 0.1
Mauna Ulu – M7	Fresh, smooth pāhoehoe	100	20	2	4.3	6.6 ± 0.1	0.72 ± 0.02	6.4 ± 0.8	0.40 ± 0.07
Mauna Ulu – M9	Fresh, smooth pāhoehoe	100	20	2	3.1	5.0 ± 0.1	0.72 ± 0.02	5 ± 1	0.8 ± 0.1
Mauna Ulu – P6	Degraded pāhoehoe	100	20	2	4.9	7.6 ± 0.1	0.73 ± 0.01	8 ± 1	0.50 ± 0.06
Mauna Ulu – P7	Degraded pāhoehoe	100	20	2	5.0	8.8 ± 0.1	0.77 ± 0.03	8.1 ± 0.3	0.72 ± 0.02
Mauna Ulu – P8	Degraded pāhoehoe	100	20	2	4.2	7.1 ± 0.1	0.72 ± 0.03	6.9 ± 0.4	0.66 ± 0.03
Moon – Korolev X (down flow)	Impact melt	100	200	141 ^d	N/A	N/A	N/A	2.2 ± 1.5 ^e	0.81 ± 0.06 ^e
Moon – Korolev X (cross flow)	Impact melt	100	200	141	N/A	N/A	N/A	2.2 ± 1.5 ^e	0.85 ± 0.05
Ina D	Lunar lava flow	100	200	141	N/A	N/A	N/A	1.5 ± 0.7 ^f	0.8 ± 0.1

^a The errors reported here are the standard deviation of all step sizes.

^b C_s and H were calculated for step sizes between 0.25 and 2 m. The errors reported here are standard errors from the fit.

^c C_s and H were calculated for step sizes between 2 and 12 m. A low pass filter was applied to the COTM, Iceland, and Hawai'i data.

^d The reported vertical precision error from SOCET SET is 1.41 m, meaning 95% of the elevation values in the DTM are internally accurate to within 1.41 m. See [Henricksen et al. \(2016\)](#) for details.

^e These values represent the average of all profiles analyzed in the area indicated in [Fig. 11](#), with 1 sigma standard deviation given as error.

^f These values represent the average of all profiles analyzed in the area indicated in [Fig. 18](#), with 1 sigma standard deviation given as error.

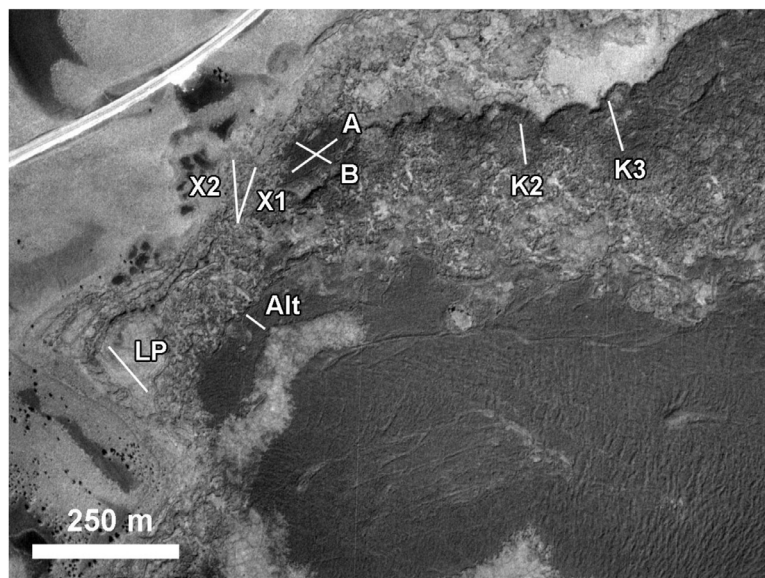


Fig. 1. National Aerial Photography Program black-and-white image (ID: O4311336.NES.836351) of North Crater and Big Craters flows at Craters of the Moon National Monument and Preserve. White lines indicate the location of eight dGPS profiles analyzed in this work. U.S. Highway 26 is visible at top left, and North is up.

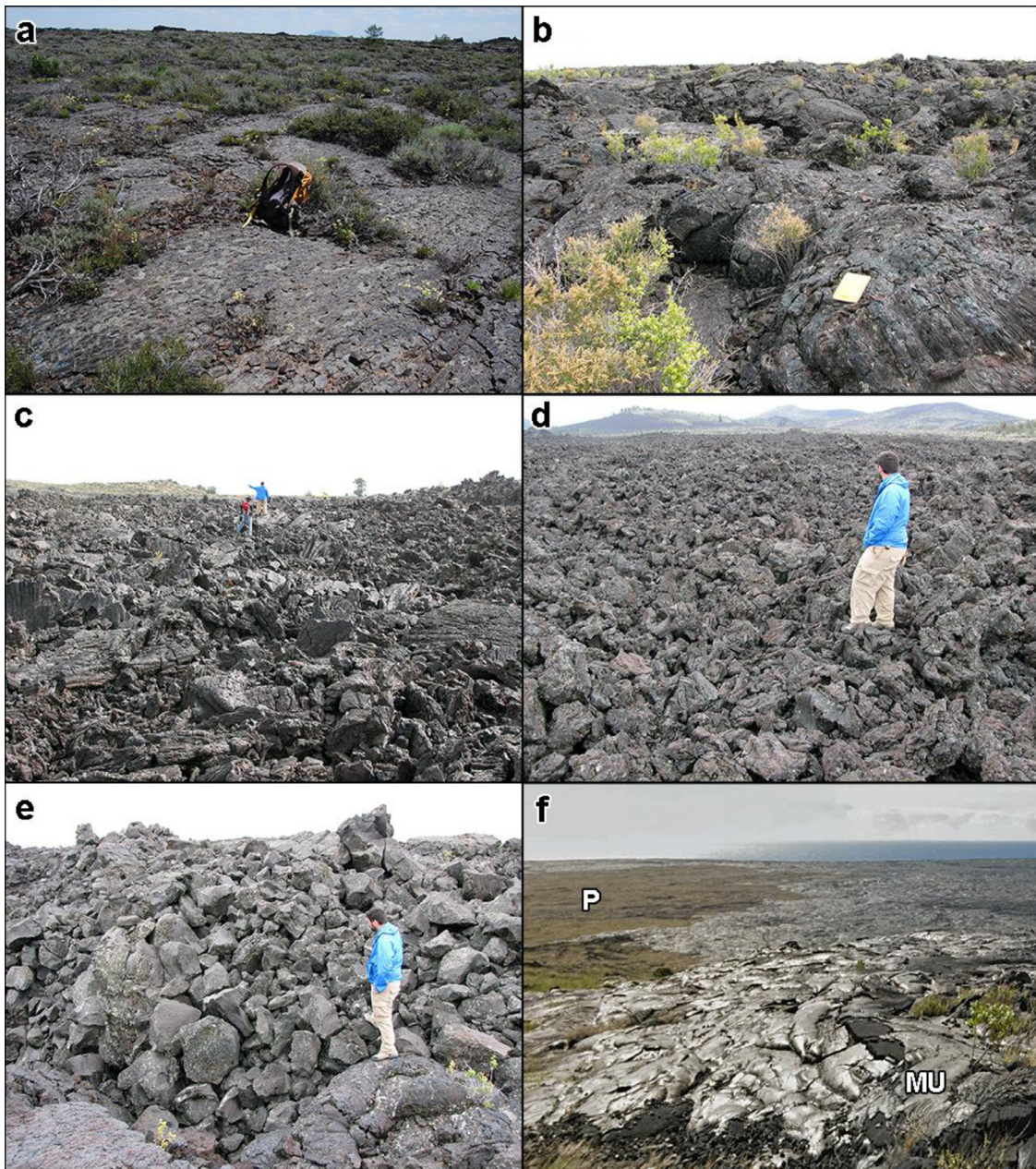


Fig. 2. Lava flow types investigated at COTM and Hawai'i: (a) The lava pond at COTM, with backpack for scale, (b) billowy pāhoehoe at COTM, with 18 cm long field notebook in foreground for scale, (c) slabby lava, (d) rubbly lava, (e) and blocky lava at COTM, with ~1.75 m tall person for scale, and (f) prehistoric (P) and modern day (MU) pāhoehoe flows at Mauna Ulu.

km² (Gíslason et al., 2015). This makes the 2014–2015 event the largest flood lava eruption to have occurred in Iceland within the last 230 years.

The resulting lava flow consisted mainly of 'a'ā and 'shelly pāhoehoe' near the vent and 'spiny' to 'rubbly' lava in the medial to distal portions of the flow. Spiny lava is characterized by a network of interconnected lobes that form inflated sheet-like flow units with rough spinose surfaces. The millimeter-scale spines on the surface of these flows resembles the texture of 'a'ā, but the flow surfaces are generally continuous and are not decomposed into clinker. In some locations, the surface of the spiny lava has been disrupted into large (meter to tens of meter-scale) plates with banded inter-plate material resembling the 'toothpaste' lava described by Rowland and Walker (1987). 'Rubbly' lava also forms inflated lobes and sheet-like units, but its surface consists of

decimeter-scale blocks of fragmented pāhoehoe-like crust, which exhibit evidence of brittle fracture along their surfaces. This formation mechanism contrasts with the development of 'a'ā clinker, which involves continuous viscous tearing of the lava surface. Spiny lava units are the dominant flow type along most of the flow margins, except near the NE margin of the flow, where rubbly lava units are locally more common in regions where the lava was confined by the east bank of a tributary to the Jökulsá á Fjöllum river. Rubbly lava units within the Holuhraun lava flow are distinct from those within the COTM lava in that the rubble is slightly larger in scale and is more angular. These lava flows were analyzed in the manner described above, and the values for RMS height, RMS slope, and Hurst exponent are reported in Table 1.

We then determined the Hurst exponent and RMS slope for an impact melt flow emanating from a lunar crater on the rim of

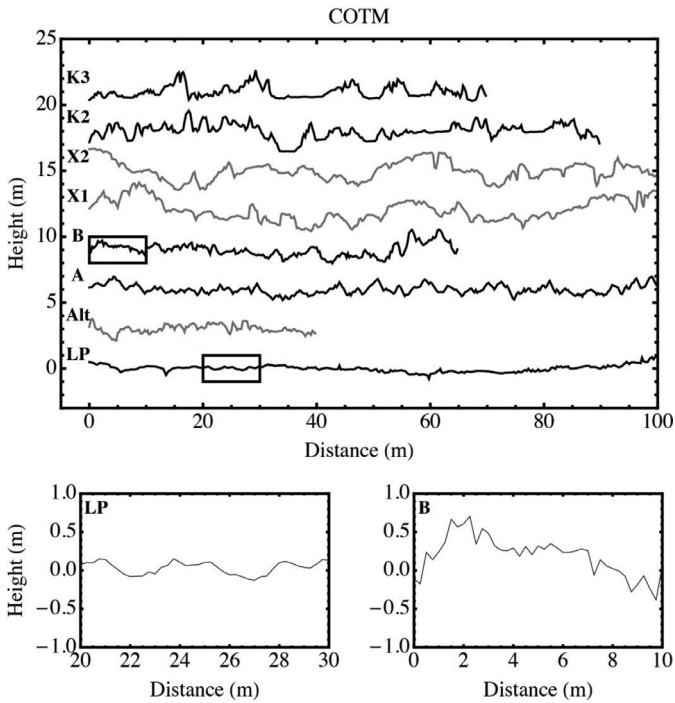


Fig. 3. (top) Eight topographic profiles representing five different lava types at North Crater and Big Craters flows in Craters of the Moon National Monument and Preserve. Labels correspond to the profile lines in Fig. 1. From bottom to top, the lava types represented are lava pond (LP), rubbly (Alt), slabby (A, B), billowy (X1, X2), and blocky (K2, K3). The best-fit linear trend has been removed from each profile, and they have been offset from each other for clarity. (bottom) The two regions outlined in black above are plotted to show the centimeter scale roughness of the lava pond (left) and the slabby lava flow (right).

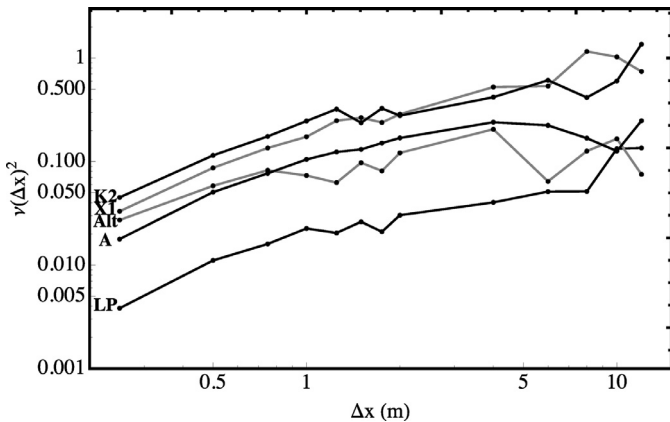


Fig. 4. Variogram plots for each of the five different lava types found at North Crater and Big Craters flows. Points are plotted every 25 cm between 0.25 and 2 m, and every 2 m between 2 and 12 m. The y-intercept is related to the RMS slope of the flow. Thus, the lava pond has the lowest RMS slope and the blocky lava has the highest RMS slope.

Korolev X (Osinski et al., 2011; Denevi et al., 2012; Neish et al., 2014). High resolution (2 m per pixel) digital terrain models (DTM) can be produced using LRO NAC data, and a handful of DTMs over lunar impact melt flows have been made publicly available through the Planetary Data System. Of the publicly available DTMs of impact melt flows, the melt flow at Korolev X is the largest and best preserved example (Fig. 9). This melt flow has radar properties typical of melt flows around other fresh craters on the Moon (Neish et al., 2014), making this an excellent type example for this study. However, in the future, comparisons between DTMs of impact melt flows in a range of degradation states are needed.

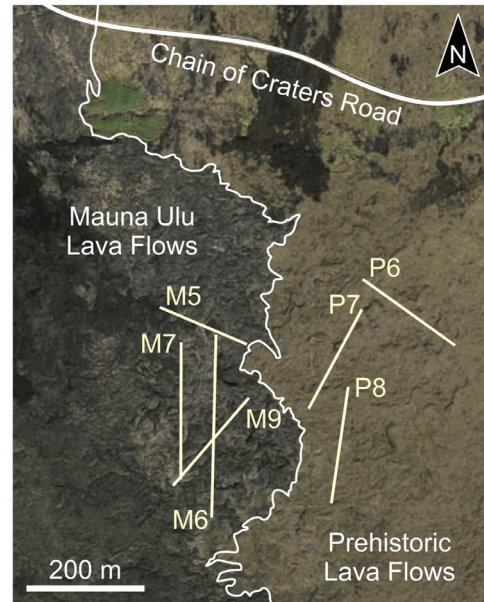


Fig. 5. Image showing a portion of the Mauna Ulu lava flow and adjacent prehistoric lavas within the Hawai'i Volcanoes National Park. Yellow lines indicate the location of the dGPS profiles analyzed in this work. These profiles all sample inflated and hummocky pāhoehoe flows. The margin of the Mauna Ulu lava flow is outlined by the thin white line. The image is centered on 19°17'16.51"N, 155° 8'38.46"W (Google Earth Imagery Date: 1/22/2013).

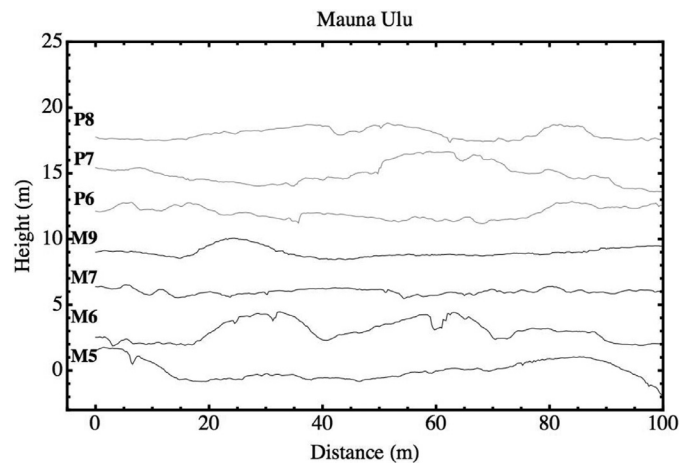


Fig. 6. Seven topographic profiles representing two different lava types at the Mauna Ulu lava flow in Hawai'i Volcanoes National Park. Labels correspond to the profile lines in Fig. 5. From bottom to top, the lava types represented are Mauna Ulu pāhoehoe (M5, M6, M7, M9) and prehistoric pāhoehoe (P6, P7, P8). The best-fit linear trend has been removed from each profile, and they have been offset from each other for clarity.

The analysis of the surface texture of the impact melt flow differed from that of the terrestrial lava flows, since we had a two-dimensional DTM rather than a one-dimensional topographic profile. In this case, we extracted a series of one-dimensional 100 m long profiles from the DTM, in two perpendicular directions – down flow and cross flow (see two example profiles in Fig. 10). From each profile, we removed the best-fit linear function, calculated the Allan variance at 2 m intervals for step sizes between 2 m and 12 m, and determined the Hurst exponent and RMS slope from fits to the variogram. These calculations were repeated, using a starting point that increased by one pixel, until we reached the end of the first row (or column, for the perpendicular direction). At that point, we moved to the next row (or column), and

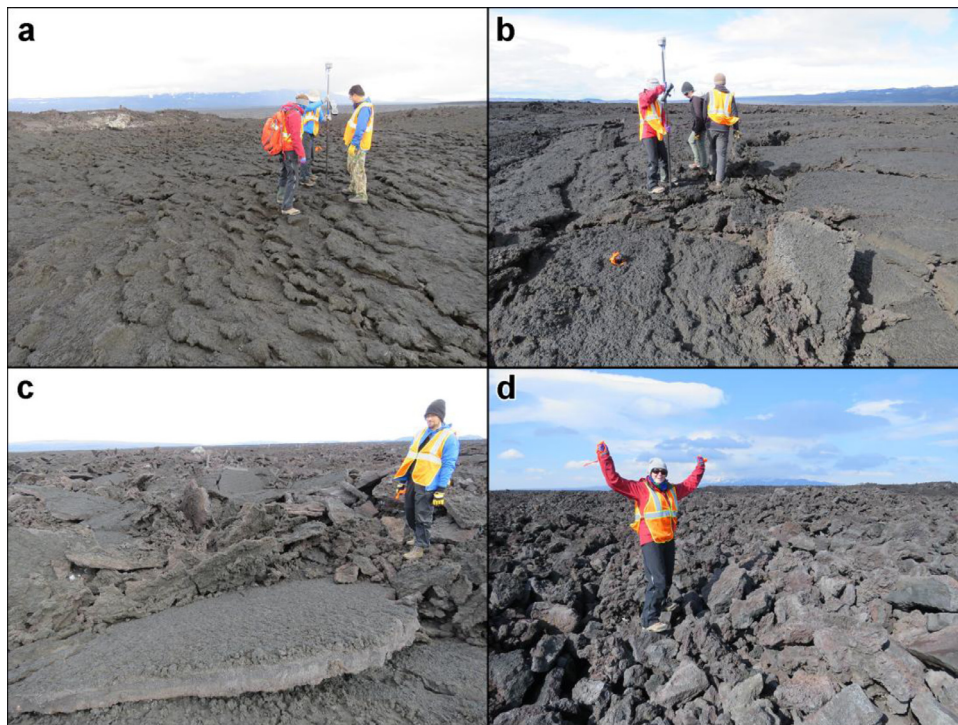


Fig. 7. Lava flow types investigated in Iceland: (a) a spiny lava pond and (b) spiny lava, with 2 m tall dGPS rover for scale, (c) slabby spiny lava, with ~1.75 m tall person for scale, and (d) rubbly lava, with ~1.5 m tall person for scale.

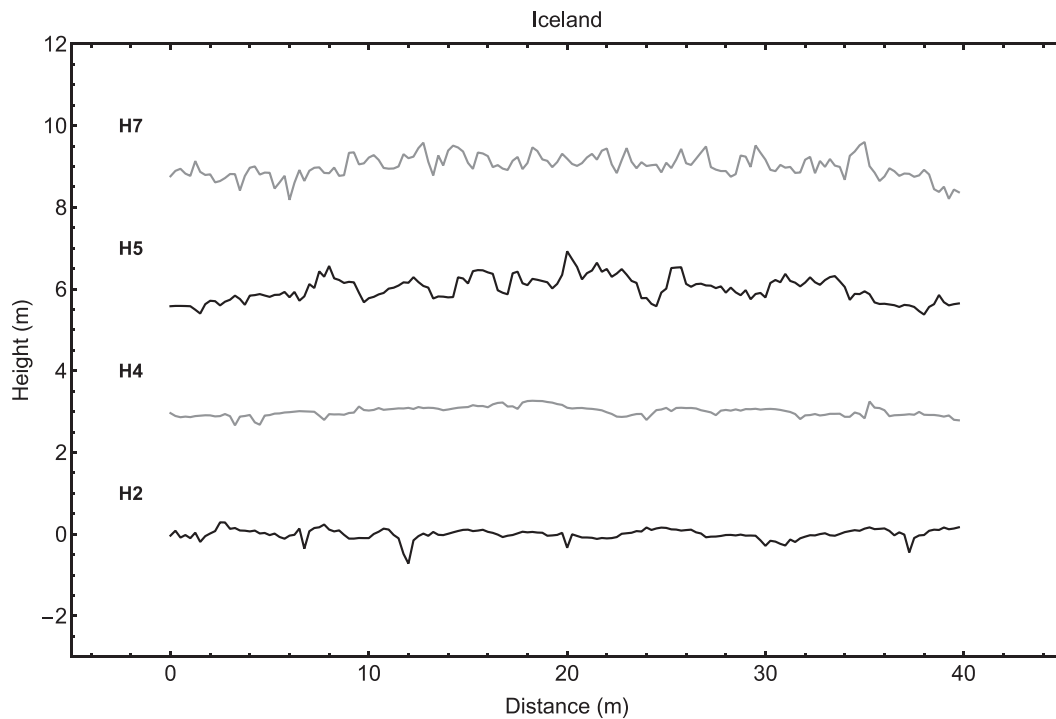


Fig. 8. Four topographic profiles representing four different lava types at the 2014–2015 Holuhraun lava flow in Iceland. From bottom to top, the lava types represented are ponded spiny pāhoehoe (H2), spiny pāhoehoe (H4), slabby spiny lava (H5), and rubbly lava (H7). The best-fit linear trend has been removed from each profile, and they have been offset from each other for clarity.

repeated the procedure, until each pixel had an associated Hurst exponent and RMS slope. We ran the completed image through a 9×9 median filter, and calculated the average Hurst exponent and RMS slope for the region indicated in Fig. 11. We found similar Hurst exponents and RMS slopes in both directions, with an aver-

age $H = 0.85 \pm 0.05$ and $C_s = 0.039 \pm 0.027$ (or 2.2°) for the cross flow direction and an average $H = 0.81 \pm 0.06$ and $C_s = 0.039 \pm 0.026$ (or 2.2°) for the down flow direction. The RMS slopes and Hurst exponents for all lava flows and impact melt flows examined in this work are plotted in Fig. 12.

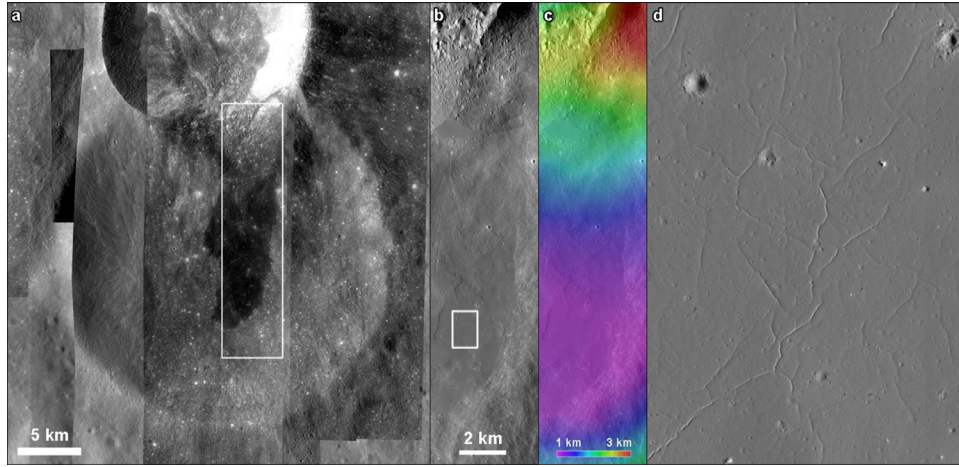


Fig. 9. (a) LRO NAC mosaic of the impact melt flow at Korolev X, overlain on the global WAC mosaic. The white rectangle shows the location of (b). (b) View of the impact melt flow, seen at higher solar incidence angle (NAC_DTM_IMPACTMELT2_M145664820_2 M.IMG). (c) Digital terrain model (DTM) of the impact melt flow, produced at a resolution of 2 meters per pixel (NAC_DTM_IMPACTMELT2_E010N2010.IMG). (d) Close-up of the region indicated by the white box in (b).

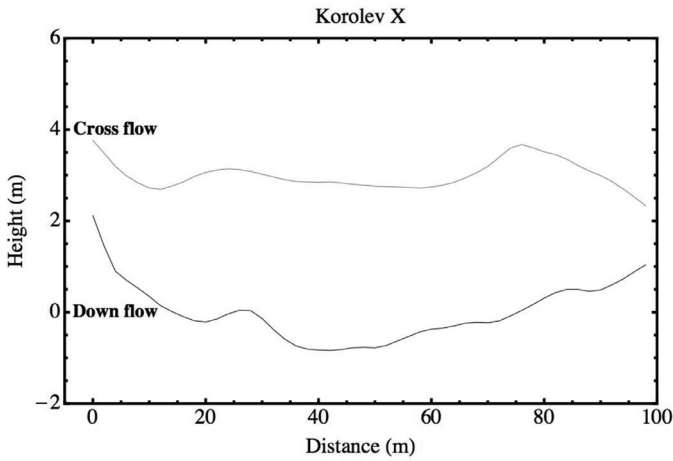


Fig. 10. Two randomly selected topographic profiles from the impact melt flow at Korolev X, taken in two perpendicular directions: down flow, and cross flow. The best-fit linear trend has been removed from each profile, and they have been offset from each other for clarity.

3. Surface roughness from radar data

Surface roughness can also be assessed using synthetic aperture radar (SAR) images. Imaging radars typically operate at wavelengths of centimeters to decimeters, so they are sensitive to surface roughness at a similar scale. There are many regions in the solar system (including the Earth) for which centimeter scale topography is difficult to obtain. Thus, linking radar backscatter to the high-resolution topographic profiles described in Section 2 is key to understanding the structure of various geologic units and how different surfaces originate and evolve with time.

To quantify roughness on different surfaces, we use the circular polarization ratio (CPR). This is defined as the ratio of the radar backscatter in the same polarization that was transmitted (SC) to the opposite polarization (OC) (i.e., $CPR = SC/OC$). For example, if a left circularly polarized wave was transmitted, SC would be the signal received in left circular polarization (LL) and OC would be the signal received in right circular polarization (LR). CPR is a useful indicator of surface roughness. When a circularly polarized radar wave is backscattered off an interface, the polarization state of the wave changes. Flat surfaces, dominated by single-bounce reflections, tend to have high OC returns and low CPR values. Rough

surfaces, on the other hand, are dominated by multiple-bounce reflections. They tend to have approximately equal OC and SC returns, with CPR values approaching one.

Rarely, CPR values can exceed one. Circular polarization ratios greater than one have been observed in rocky areas such as Maxwell Montes on Venus (Campbell et al., 1999), blocky lava flows on the Earth (Campbell et al., 1993), lava flows on Mars (Harmon et al., 2012), and fresh ejecta blankets on the Moon (Campbell, 2012). Circular polarization ratios up to 2 can be produced via multiple reflections from rock edges and cracks, while scattering from natural corner reflectors (dihedral scattering) can produce an average CPR up to 3–4 (Campbell, 2012).

We examined L-Band (24 cm wavelength) AIRSAR images of North Crater and Big Craters lava flows in COTM (Fig. 13). AIRSAR was a fully polarimetric imaging radar operated by NASA/JPL that flew on a DC-8 aircraft from 1988 through 2004 (Evans et al., 1986). It operated simultaneously at C-Band (5.6 cm), L-Band (24 cm), and P-Band (68 cm). In this work, we examine L-Band data acquired at COTM on March 31, 2003 (Khan et al., 2007).

The radar data was processed and calibrated using the AIRSAR data processor version 6.38 on May 27, 2004, and made available in compressed Stokes matrix format. The calibration corrected for channel gain imbalance, and the measured and corrected HV/VH power ratio for this scene is 1.012. The HV and VH phase difference was also measured, and used in the phase calibration of the compressed Stokes matrix pixels. We used the Stokes matrix (W) to reconstruct the SC (LL) and OC (LR) radar returns (Eqs. (8) and (9)) (Campbell, 2002). The circular polarization ratio is slightly different if RR and RL returns are used instead, but previous work has reported LL and LR returns, so that is what we report here.

$$\sigma_{LL}^0 = W_{11} + 2W_{14} + W_{44} \quad (8)$$

$$\sigma_{LR}^0 = W_{11} - W_{44} \quad (9)$$

In addition to surface roughness, factors such as vegetative cover may have affected the radar returns obtained in 2003. However, the vegetative cover on the COTM lava flows is sparse to non-existent, and no obvious changes in the vegetative cover have occurred between the time of the AIRSAR data collection in 2003 and the fieldwork conducted in 2014 (S. Hughes, personal communication). Thus, we deem this to be a negligible effect. Radar returns are also sensitive to the incidence angle of the radar. The look angle varied across the scene from 30.8° in the near range to 63.8° in the far range. The lava flows of interest were in the range of $38\text{--}44^\circ$, similar to the look angle of Mini-RF, 48° .

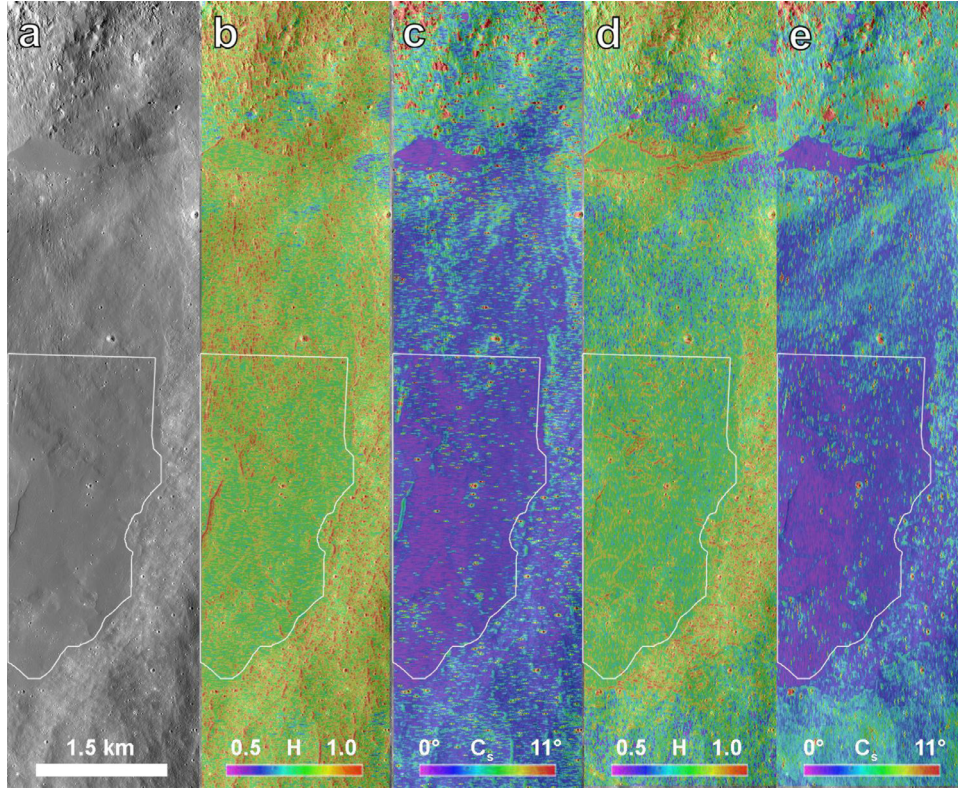


Fig. 11. Roughness properties of the impact melt flow at Korolev X. (a) LRO NAC image of the impact melt flow (NAC_DTM_IMPACTMELT2_M145664820_2 M.IMG). (b) Hurst exponent and (c) root mean square slope (C_s), calculated in the cross flow direction. (d) Hurst exponent and (e) root mean square slope, calculated in the down flow direction. Average properties of the impact melt flow were calculated from the region outlined in white. North is up.

Table 2
Radar properties of representative lava flows and a lunar impact melt.

Lava Type	Incidence angle (°)	Wavelength	$\langle LL \rangle / \langle LR \rangle$	$\langle LL / LR \rangle$
COTM Billowy	38–44	L-Band	0.31	0.44
COTM Rubbly	38–44	L-Band	0.43	0.59
COTM Blocky	40–42	L-Band	0.66	0.91
Holuhraun Rubbly	50–53	L-Band	0.47	0.51
Kīlauea 4 (billowy pāhoehoe) ^a	44	C-Band	0.29	-
		L-Band	0.29	-
Kīlauea 5 (‘a‘ā)	40	C-Band	0.37	-
		L-Band	0.49	-
Kīlauea 10 (smooth pāhoehoe)	41	C-Band	0.14	-
		L-Band	0.18	-
Impact melt at Korolev X	48	S-Band	1.1	1.3

^a Kīlauea results reported in Fig. 6.10 and 6.11 in Campbell (2002). The data reported there was a ratio of the mean LL return to the mean LR return (B. Campbell, personal communication).

For each region of interest, we determined the mean SC and OC return, as well as the mean CPR (Table 2). The $\langle SC \rangle / \langle OC \rangle$ values (a ratio of averages) are slightly lower than the $\langle CPR \rangle$ values (an average of ratios), because a few large numbers influence the latter calculation more than the former calculation. Thus, the $\langle SC \rangle / \langle OC \rangle$ value tends towards the mode of the $\langle CPR \rangle$ distribution, providing a complementary way of calculating the average CPR of the regions of interest. The AIRSAR data used had a pixel size of 5 m, and each pixel had $N = 9$ looks. The approximate uncertainty is $1/N^{1/2}$ for each pixel, or 33% (Campbell, 2002). We reduced the resolution by a factor of four (thus reducing speckle noise to 8%) and found no difference in the mean values reported here.

We also examined an L-Band UAVSAR image of the 2014–2015 Holuhraun eruption (Fig. 14). UAVSAR is a fully polarimetric air-

borne radar run by NASA/JPL that became operational in 2009 (Hensley et al., 2005). The image of the Holuhraun flow was acquired on May 30, 2015, just three months after the end of the eruption. We used the ground range projected files to calculate the Stokes matrix (Eqs. (10)–(12)) (Zebker and Lou, 1990):

$$W_{11} = \frac{1}{4} [S_{hh} \cdot S_{hh}^* + S_{vv} \cdot S_{vv}^* + 2S_{hv} \cdot S_{hv}^*] \quad (10)$$

$$W_{14} = -\frac{1}{2} \mathcal{I} [S_{hh} \cdot S_{hv}^*] - \frac{1}{2} \mathcal{I} [S_{hv} \cdot S_{vv}^*] \quad (11)$$

$$W_{44} = \frac{1}{2} S_{hv} \cdot S_{hv}^* - \frac{1}{2} \mathcal{R} [S_{hh} \cdot S_{vv}^*] \quad (12)$$

Here, \mathcal{R} and \mathcal{I} represent the real and imaginary parts of the scattering matrix elements, respectively. We then used Eqs. (8) and (9) to calculate the LL and LR returns. The ground projected files used in this work are calibrated complex cross products projected to the ground in simple geographic coordinates. The image had a pixel spacing of 5.556×10^{-5} degree per pixel (latitude) and 1.1111×10^{-4} degree per pixel (longitude). There were $N = 3$ looks in the range direction and $N = 12$ looks in the azimuth direction, and the incidence angle ranged from 46° at the toe of the flow to 65° near the vent. We determined the mean SC and OC return, as well as the mean CPR, in a region of rubbly lava outlined in Fig. 14 (Table 2). We visited the region in August 2015, less than three months after the acquisition of these radar images, so any changes that may have occurred due to weathering are minimal.

Finally, we examined an S-Band (12.6 cm wavelength) Mini-RF image of the impact melt flow at Korolev X (Fig. 13). Mini-RF was a hybrid dual-polarimetric radar, which transmitted in left circular polarization and received two coherent orthogonal linear polarizations (H and V) (Raney et al., 2012). The full Stokes vector [S_1, S_2, S_3, S_4] was determined from the total power received in the H and

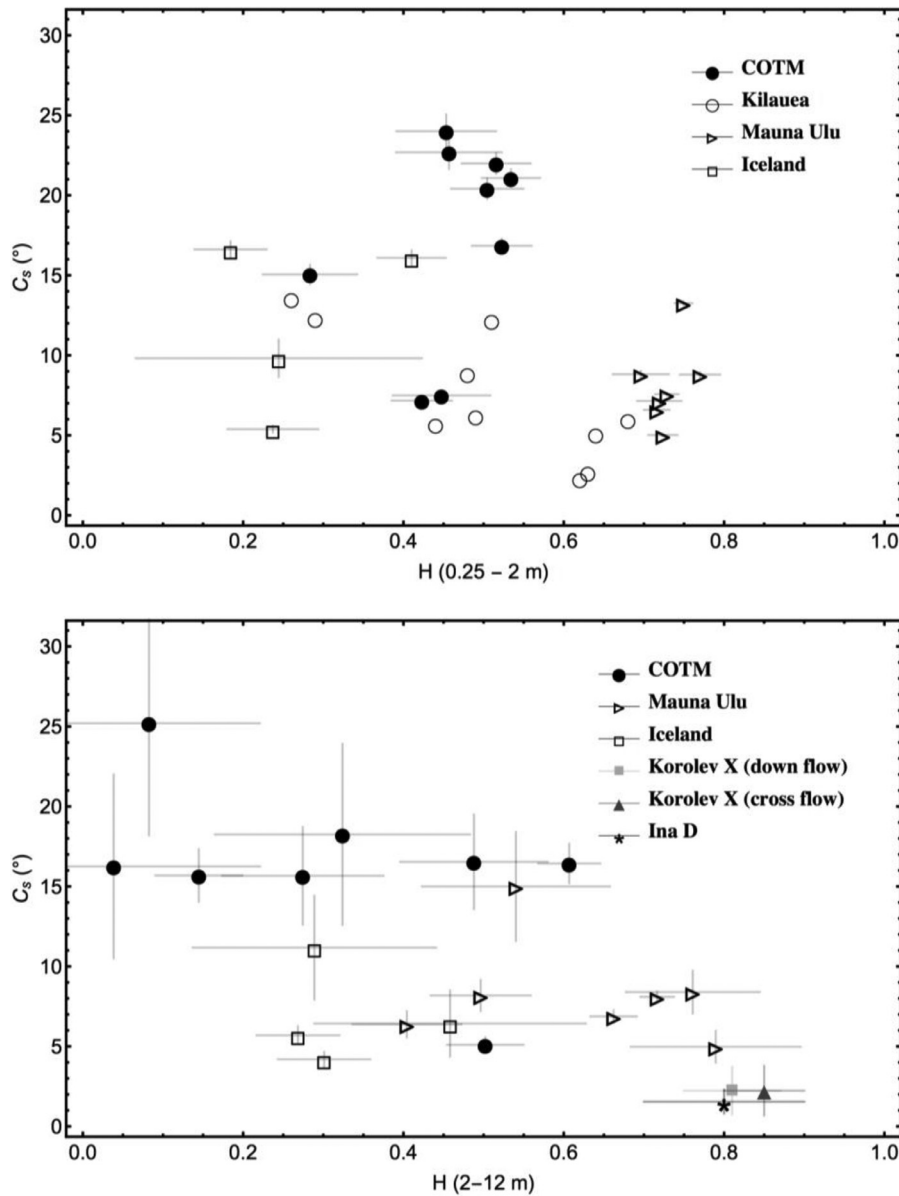


Fig. 12. Root mean square (RMS) slope at 1 m reference scale versus Hurst exponent for terrestrial lavas, a lunar lava flow, and a lunar impact melt flow over two different ranges of step size - 0.25 m to 2 m (top), and 2 m to 12 m (bottom). The data presented here are from Hawaiian lavas reported in Campbell (2002) (Kilauea), Hawaiian lavas studied in Mauna Ulu, transitional lava flows at COTM, the new lava flow at Holuhraun in Iceland, a lava flow at Ina D, and the impact melt flow at Korolev X.

V channels and the real and imaginary parts of their complex conjugate, HV^* (Raney, 2006). Mini-RF had a fixed look angle of 48° (similar to the incidence angles in the AIRSAR and UAVSAR regions of interest), and the Mini-RF images were calibrated and processed with a pixel size of 7.5 m, each with an effective number of looks equal to $N \approx 7$. The data was reduced to a pixel spacing of 15 m before analysis, giving speckle noise of $1/N^{1/2} \approx 19\%$ for each pixel. We determined the mean $SC = S_1 - S_4$ and $OC = S_1 + S_4$ return, as well as the mean CPR, in a region of the impact melt at Korolev X (Table 2). The CPR values observed at this crater are similar to those observed for impact melt deposits around other lunar craters (Campbell et al., 2010; Carter et al., 2012; Neish et al., 2014).

The results are summarized in Table 2, along with CPR values for three sites in Kilauea that were discussed in Section 2 (Campbell, 2002). The transitional basaltic lava flows at COTM and Holuhraun generally have larger mean CPRs than the Hawaiian lavas, but only the blocky lava approaches the CPR value of the impact melt deposit, which generally exceeds one. However,

caution should be exercised when comparing the radar returns of AIRSAR and UAVSAR to those of Mini-RF. The CPR values cannot be directly compared, since the wavelengths differ by a factor of two (12.6 cm vs. 24 cm). However, an average of C- and L-Band backscatter can be used to give a simulated S-Band value (Shepard et al., 2001). We find only modest differences in CPR for the C-Band and L-Band data reported in Campbell (2002) for the sites in Kilauea: the CPR for Site 4 is 0.29 at C-Band versus 0.29 at L-Band, the CPR for Site 5 is 0.37 at C-Band versus 0.49 at L-Band, and the CPR for Site 10 is 0.14 at C-Band and 0.18 at L-Band. No usable C-Band data is available over Holuhraun, and work is ongoing to determine the differences in response at C-Band and L-Band at COTM (Zanetti et al., 2016). If the behavior is similar to that reported for the sites in Kilauea, the L-Band data should be a reasonable proxy for the S-Band returns from the Moon, although it will be sensitive to roughness of a slightly larger scale than the Mini-RF data.

Another issue that may complicate comparisons between terrestrial radar data and Mini-RF data is that the S-Band CPR

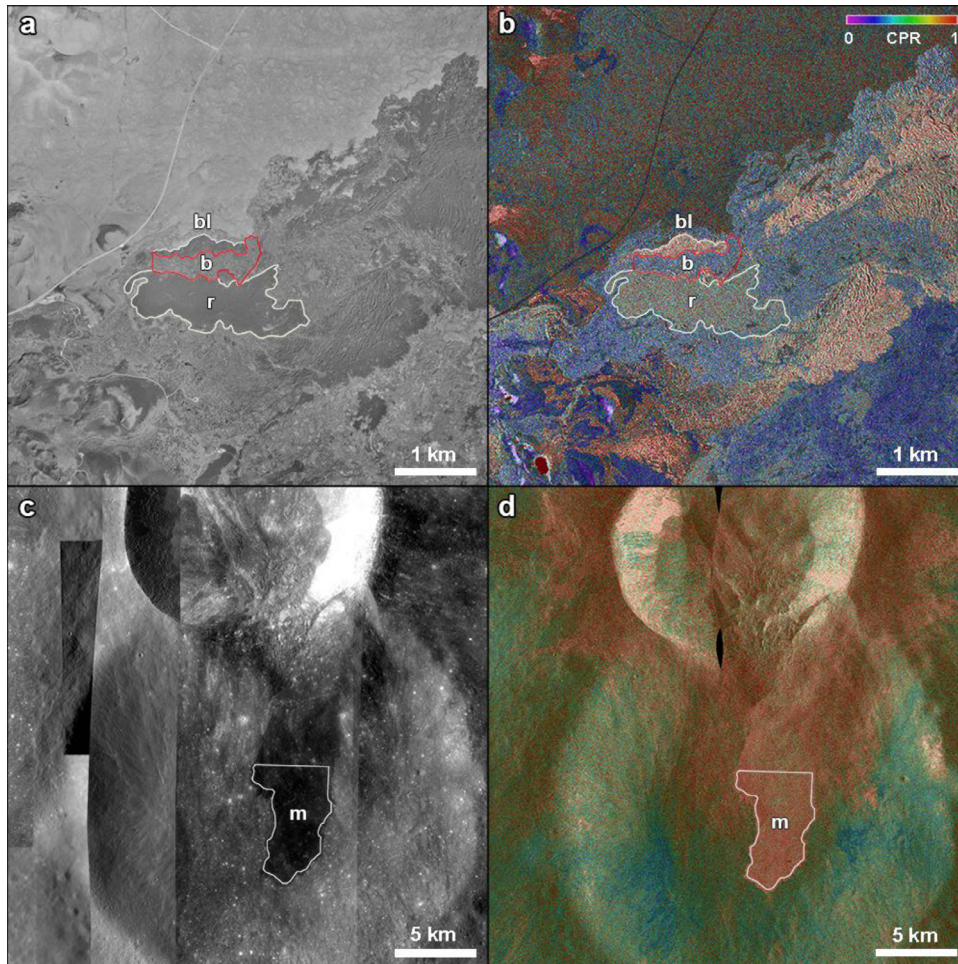


Fig. 13. (a) National Aerial Photography Program black-and-white image (ID: O4311336.NES.836351) of North Crater and Big Craters flows at Craters of the Moon National Monument and Preserve. Representative areas of rubby (r), billowy (b), and blocky (bl) lava types are outlined. (b) AIRSAR L-Band image of the same region. Colorized circular polarization ratio is overlaid on a total radar backscatter (S1) image. (c) LRO NAC mosaic of the impact melt flow at Korolev X, overlain on the global WAC mosaic. An area of impact melt (m) is outlined. (d) Mini-RF S-Band image of the same region. Colorized circular polarization ratio is overlaid on a total radar backscatter (S1) image. North is up in all images.

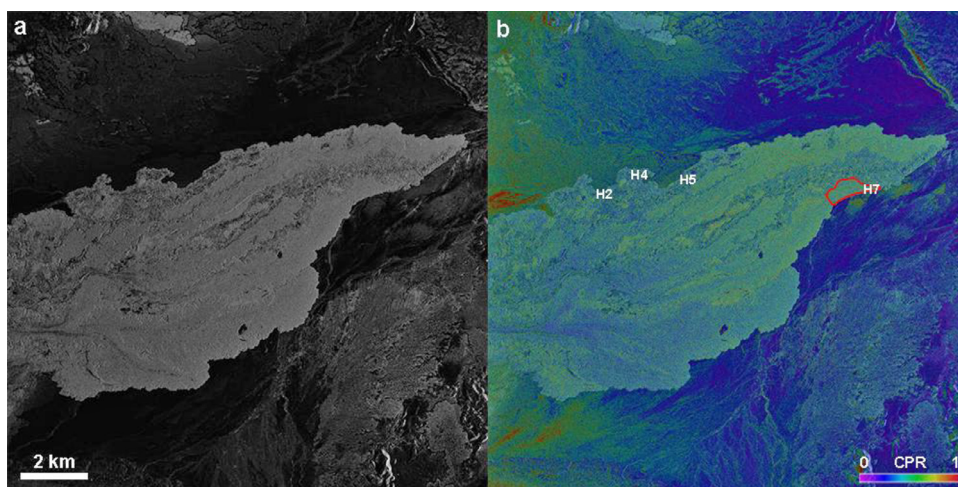


Fig. 14. (a) UAVSAR L-Band total radar backscatter (S1) image of the lava flow produced during the 2014–2015 Holuhruan eruption in Iceland. The center coordinates are 64.9°N, 16.6°W, and north is up. (b) Colorized circular polarization ratio (CPR) overlaid on the total radar backscatter image. The locations of the four transects are marked (see Table 1). An area of rubby lava is outlined in red, and the average circular polarization ratio is reported in Table 2.

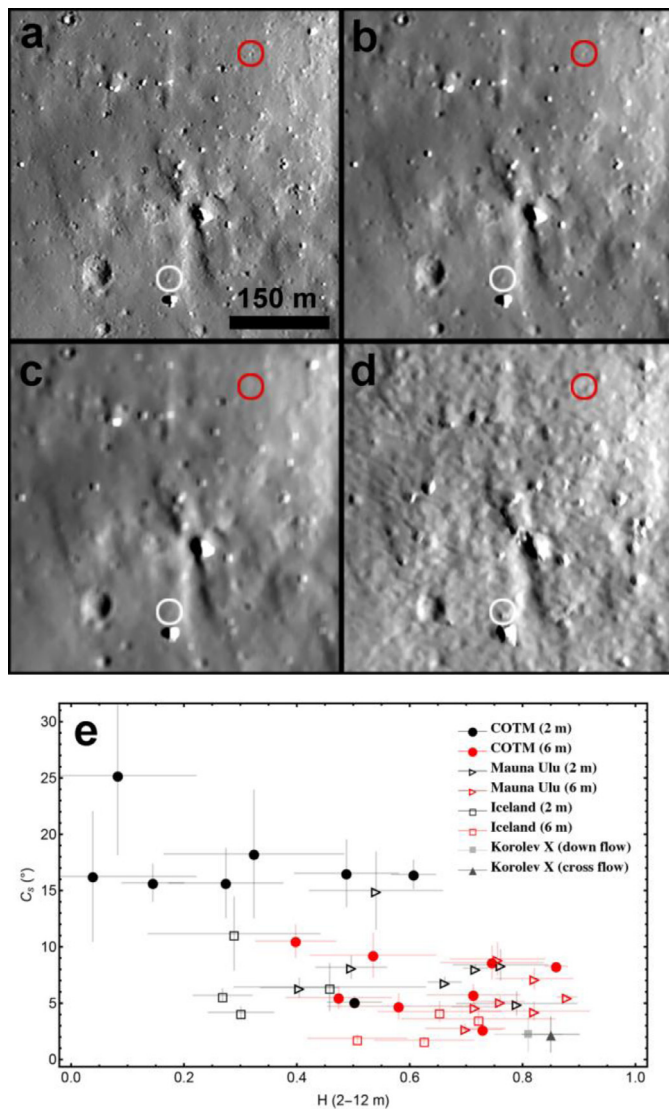


Fig. 15. (a) A portion of a NAC image of a lunar impact melt flow (NAC_DTM_IMPACTMELT2_M145664820_2.M.IMG), showing the data at 2 m/pixel resolution. (b) The same data set reduced to 6 m/pixel and (c) 10 m/pixel by applying a lowpass filter. (d) A shaded relief image of the NAC DTM (NAC_DTM_IMPACTMELT2_E010N2010.IMG), using the same illumination conditions as the original image. Features marked in white circles in (a) and (b) are observed in (d) but not (c), while features marked in red circles are obvious in (a), difficult to observe in (b) and (d), and not present in (c). This suggests an effective resolution less than 2 m, but more than 10 m. (e) When the dGPS profiles are reduced in resolution to 6 m, they tend to produce results with higher Hurst exponents and lower RMS slopes. (For interpretation of the references to colour in this figure legend, the reader is referred to the web version of this article.)

values obtained from Mini-RF are observed to differ from those obtained from ground based S-Band radars. The Mini-RF CPR is consistently lower than those obtained from the bistatic combination of the Arecibo Observatory radar transmitter and the Green Bank Telescope (GBT) receive system, even when acquired at similar incidence angles (Carter et al., 2014). The reason for this discrepancy is not presently known, but is probably a combination of factors including compression errors, differences in the transmit axial ratio, and the choice of transmit and receive basis for the compact polarimetry. Indeed, the reconstruction of certain scattering parameters from a dual-polarimetric radar (e.g., Mini-RF, Arecibo/GBT) can vary depending on the choice of transmit and receive basis (Nord et al., 2009). These concerns will be addressed in future work [e.g., Carter et al., 2016].

However, we can say that impact melt flows have higher values of CPR than most other lunar materials (except for fresh impact crater ejecta), and this is true for observations made by both Mini-RF (Carter et al., 2012; Neish et al., 2014) and Arecibo (Campbell et al., 2010). The increased CPR may be a result of either a large number of wavelength-sized cracks or a large number of wavelength-sized blocks. (If the block sizes are significantly larger or smaller than the radar wavelength, they have qualitatively lower values of CPR (Bulmer et al., 2005; Campbell et al., 2009a).) Meter scale cracks are observed in many lunar impact melt flows (see Fig. 9d), so it is reasonable to assume that smaller, decimeter scale cracks may also be present. Scattering from cracks can produce CPR of one for single scattering, and up to two for multiple reflections (Campbell, 2012). However, larger increases in CPR (up to 3–4) requires scattering from natural corner reflectors (the dihedral mechanism), formed by pairs of rock faces (such as you might find in a blocky flow). Campbell (2012) judge that only the dihedral mechanism is capable of producing the highest CPR values observed on the Moon. This is consistent with observations of lava flows on Earth – the only terrestrial lava flows with CPRs that exceed one have a blocky texture, like SP Flow in Arizona (Campbell et al., 1993), or the blocky flows studied in Idaho (Fig. 13). Many terrestrial lava flows have decimeter-scale cracks, but show no associated increase in circular polarization ratio (see, for example, the billowy lavas in Fig. 13). Therefore, one reasonable interpretation of the Mini-RF data is that lunar impact melts have a surface or near-surface texture that consists of decimeter scale blocks.

4. Discussion

In this work, we sought to identify terrestrial lava flows that possess analogous surface properties to lunar impact melt flows, in terms of having similar radar polarization ratios, Hurst exponents, and root mean square slopes. We examined lava flows that ranged in texture from smooth Hawaiian pāhoehoe to blocky and slabby transitional basaltic lava flows at COTM to rubbly and spiny lava at Holuhraun in Iceland. At the decimeter scale, lunar impact melts look most like blocky lava flows, but at the meter scale, they appear most like smooth Hawaiian pāhoehoe. No terrestrial analogue yet studied appears to have the same small-scale roughness coupled with large-scale smoothness observed in lunar impact melt deposits. The closest analogue observed to date is the months old rubbly lava at Holuhraun. This lava flow is observed to have both (a) moderate values of CPR and (b) comparable values of root mean square slopes at the meter scale. However, even this lava flow does not have similarly large values of the Hurst exponent ($H = 0.5 \pm 0.2$ vs. average values of $H = 0.8 \pm 0.1$) or the extreme values of circular polarization ratio (~ 0.5 vs. > 1) observed in lunar impact melt flows.

How, then, do we reconcile the unusually ‘rough’ radar returns of lunar impact melt flows at decimeter scales with the ‘smooth’ appearance at meter scales? Why are the surface properties of lunar impact melt flows unlike any terrestrial lava flow yet studied? We explore several different explanations below, which roughly cluster into three groups: (1) differences in data processing, (2) differences in post-emplacement modification processes, and (3) fundamental differences in the surface texture of the melt flows due to the melts’ unique emplacement and/or cooling environment.

4.1. Differences in data processing

The observed differences between lunar impact melt flows and terrestrial lava flows may be a consequence of our chosen method of data processing. It is possible our results were artificially biased by the manner in which we chose to downsample our terrestrial data to mimic its lunar counterpart. To determine the sensitivity of

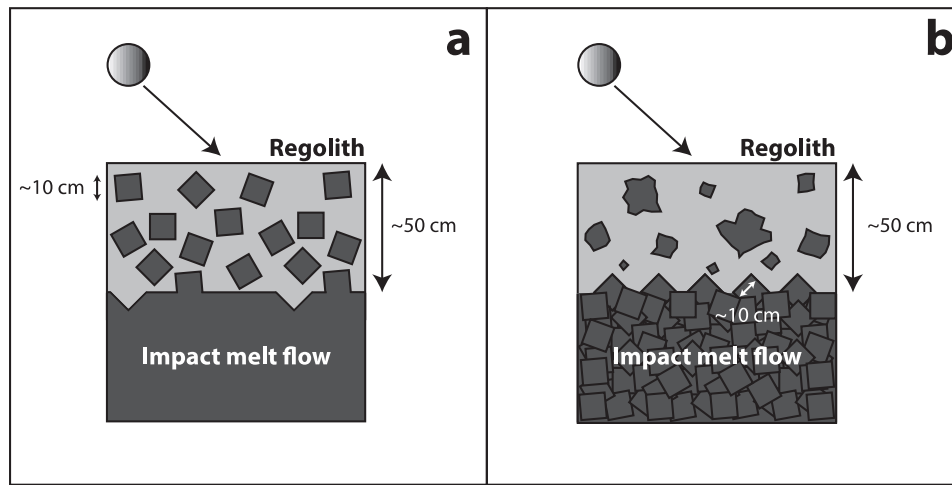


Fig. 16. Two hypotheses to explain the observed physical properties of lunar impact melt deposits (shown in dark gray). The regolith development (shown in light gray) represents a ~500 Myr old crater. Younger melt flows would have less regolith, and older melt flows would have more. (a) Impact melt flows originally have a surface texture similar to terrestrial lava flows. The surface is disrupted through impact gardening to produce an abundance of decimeter scale blocks. The blocks cause double-bounce backscatter, leading to high CPR. (b) Impact melt flows are formed with an unusual surface texture, blocky at the decimeter scale but smooth at the meter scale, producing high CPR returns at S-Band. Impact gardening would disrupt these deposits as well, exposing additional blocky terrain below, but the products of the disruption are not required to be predominantly decimeter scale blocks.

the results to the choice of low pass filter used, we computed the Hurst exponent and RMS slopes for profiles that were subjected to different low pass filters. In addition to the moving average of eight elements spaced 25 cm apart, we also computed the moving median of eight elements, and two successive moving averages of four elements. These gave the same results as those computed with the original low pass filter, within errors.

We also investigated the sensitivity of the results to the length of the low pass filter. [Henricksen et al. \(2016\)](#) found that the horizontal uncertainty of NAC DTMs is consistently less than the pixel size of 2 m. However, the effective resolution may be slightly lower than 2 m due to artifacts of the algorithm used to generate the DTM. To determine the effective resolution of the DTM, we generated images of the melt flow with reduced resolutions (using the 'lowpass' application in the ISIS 3 software package), and compared them to a shaded relief image of the DTM, produced with identical illumination conditions. Qualitatively, we found that we could identify features in the shaded relief image with the same accuracy as we could in the image reduced to a resolution of 6 m/pixel.

In general, we find that reducing the effective resolution of the resulting topographic profiles (a) increases the derived Hurst exponent and (b) decreases the RMS slope ([Fig. 15e](#)). However, even if we use an effective resolution of 6 m, in only a few cases did the results overlap with those observed for the lunar impact melt flow, and the majority of these are smooth pahoehoes with distinct radar returns to the melt flows. The most intriguing analogue remains the rubbly lava from the recent eruption in Iceland (although here too the measured CPR is considerably less than that observed for melt flows on the Moon). Photoclinometry based on the original, higher resolution NAC image would provide topographic profiles more comparable to the terrestrial profiles acquired in the field, and an analysis of this type would be worth exploring in future studies.

4.2. Differences in post-emplacement modification processes

Terrestrial lava flows and lunar impact melts are also subject to very different post-emplacement modification processes, which may account for their observed differences. For example, the erosional environment on the Moon is quite different than that encountered on the Earth. The surface of the Moon is pri-

marily altered through impact gardening, while the surface of the Earth is subject to a wide range of landscape modification processes, including fluvial degradation and aeolian infilling. However, the erosion of lava flows on the Earth is unlikely to be the sole cause of the observed roughness differences. For example, a pristine, months old lava flow in Iceland failed to replicate all of the observed characteristics of lunar impact melt flows. In addition, the lava flows at COTM are much rougher than the younger lava flows in Iceland and Hawai'i, suggesting that smoothing through erosion has only a secondary effect on decimeter and meter scale surface roughness over these timescales (at least in the unvegetated environments encountered in the three study regions).

Alternatively, the radar may be sensing the disrupted surface of the melt flow, broken apart by impact gardening and covered with regolith ([Fig. 16a](#)). The buried blocks would be visible to a radar, which can probe the near subsurface (up to ~10 times the radar wavelength in lunar regolith), but not to an optical or infrared camera, which is only sensitive to the top few microns of the surface. Shallowly buried blocky crater ejecta can remain undisturbed for long periods of time ([Ghent et al., 2016](#)), so the same may be true for disrupted melt flows.

The presence of a nearly uniform regolith cover is supported by an analysis of the Diviner brightness temperature data over the melt flow at Korolev X. Large temperature differences between spectral channels indicate a large variety of temperatures in the Diviner field of view, which typically indicates increased surface roughness at the ~0.5 cm scale ([Fig. 17](#); see [Bandfield et al. \(2015\)](#) for a detailed description of this technique). This effect is most pronounced when the sun is low to the horizon, before 1000 H or after 1400 H local time. [Fig. 17](#) hints that the temperature difference over the melt flow is similar to typical highlands terrain. This implies that the Korolev X melt flow surface has a broadly similar surface texture compared to other lunar surfaces at the centimeter scale (~20° RMS slope distribution ([Bandfield et al., 2015](#))). In addition, the Korolev X melt flow has low rock abundance values consistent with a surface dominated by regolith cover ([Bandfield et al., 2011](#)). The average rock abundance in the melt region shown in [Fig. 17](#) is an order of magnitude lower than the highest rock abundance in the area (~1.3% vs. ~29.8%). The latter values are more typical of boulder-sized rocks exposed at the

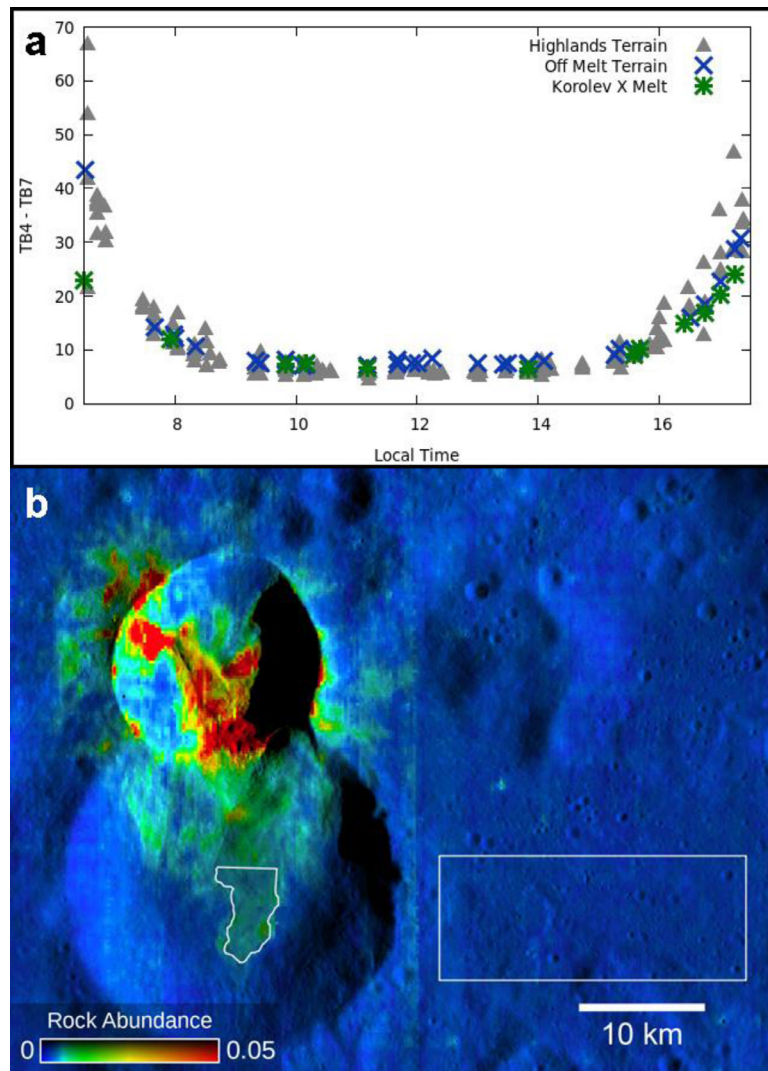


Fig. 17. (a) Brightness temperature difference between Diviner bands 4 and 7 as a function of local time. Three different regions are represented: typical highlands terrain (gray triangle), the impact melt flow at Korolev X (green star), and a relatively featureless area just east of Korolev X (blue x). Larger differences in brightness temperature typically represent increased surface roughness. (b) Diviner rock abundance data overlaid on a LRO WAC DEM shaded relief image. White outlines define the regions used to derive surface roughness for the 'Korolev X Melt' and 'Off Melt Terrain' shown in (a). The 'Highlands Terrain' region is described in [Bandfield et al. \(2015\)](#). (For interpretation of the references to colour in this figure legend, the reader is referred to the web version of this article.)

surface. The low rock abundance over the melt flow thus suggests the presence of a fine particulate layer.

We can test the hypothesis that Mini-RF is sensing the disrupted surface of melt flows through comparisons to young mare lava flows. If the radar return is produced by the formation of decimeter scale blocks through impact gardening, lunar lava flows of similar ages (i.e. Copernican and Eratosthenian) should show similar behavior. They do not. The youngest mare surfaces have lower CPR than the oldest mare surfaces, and the mare in general have lower CPR than highlands terrain ([Cahill et al., 2014](#)). There are rough mare lava flows observed in P-Band (70 cm wavelength) radar images of the Moon ([Campbell et al., 2009b](#)), but these tend to be buried such that they are not visible to S-Band radars. It is unclear why only older, buried lava flows would show high CPR. It may be that the higher TiO_2 abundance in the mare attenuates the S-Band radar wave before it reaches the boundary between the flows and the regolith. Since the older mare generally have low TiO_2 and the younger mare generally have higher TiO_2 , it is possible the relation is simply due to radar attenuation, not the flow texture ([Campbell et al., 2014](#)).

However, even the youngest mare lava flows on the Moon, some of which may be as young as tens of millions of years old ([Braden et al., 2014](#)) have low CPR ([Carter et al., 2013](#)). This suggests that at least some mare flows have different surface properties than impact melt flows. An interesting analogue site is the Ina D depression, located at 18.66°N and 5.30°E on the near side of the Moon ([Fig. 18](#)). This feature has been interpreted to be an extremely young, irregular mare patch with a crater retention age of 33.2 ± 2 Myr ([Braden et al., 2014](#)). Thus, although it has a similar age to impact melt flows around young, fresh craters, it was likely formed through volcanic processes rather than impact related processes. A high-resolution (2 m/pixel) DTM is available for Ina, which we analyzed using the same techniques applied to the DTM for the impact melt at Korolev X. For one prominent lava flow (marked by a white box in [Fig. 18](#)), we found a mean Hurst exponent $H = 0.8 \pm 0.1$ and a mean RMS slope of $C_s = 0.027 \pm 0.013$ (or 1.5°). (The results were the same for both perpendicular directions shown in [Fig. 18](#).) These characteristics suggest Ina D has similar physical properties to the flow profiles taken at Korolev X (i.e., smooth at the meter scale). However, when viewed at radar wavelengths ([Fig. 18c](#) and [d](#)), Ina D looks similar to the

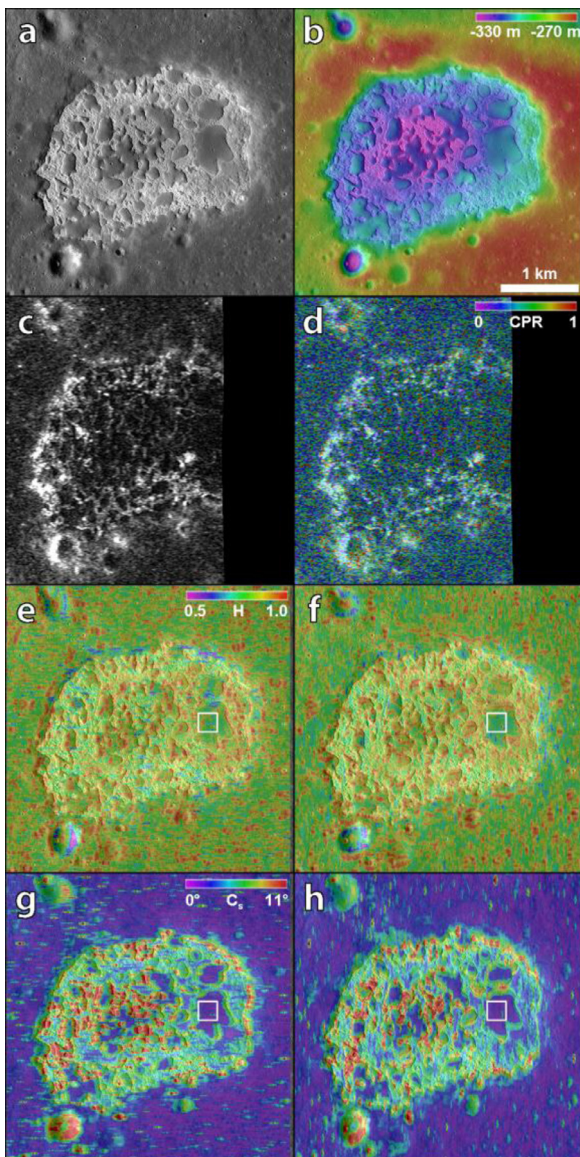


Fig. 18. (a) LRO NAC mosaic of the Ina D depression (NAC_DTM_INACALDERA_MOSAIC_2 M.IMG). (b) Digital terrain model of the irregular mare patch, produced at a resolution of 2 meters per pixel (NAC_DTM_INACALDERA_E190N0050.IMG). (c) Mini-RF S-Band total radar backscatter (S1) image of the same region. The black region was not imaged by Mini-RF. (d) Colorized circular polarization ratio (CPR) is overlaid on the S1 image. (e, f) Hurst exponent (H) and (g, h) root mean square slope (C_s) for this region, determined in two perpendicular directions. (In (e) and (g) the profiles go from left to right, in (f) and (h) the profiles go from top to bottom.) The white box shows the area used to characterize the mean physical properties of one lava flow, as described in the text. North is up in all images.

surrounding regolith. It thus appears to have roughness properties at the decimeter scale that differ from those of lunar impact melt flows. Thus, we think it is unlikely that the unusual physical properties of impact melt flows can be simply attributed to the impact gardening of a solid melt on the lunar surface.

4.3. Fundamental differences in the surface texture

A final, more speculative explanation is that impact melt flows have a fundamentally different surface texture than lava flows on Earth, due to their unique emplacement or cooling conditions (Fig. 16b). Unlike terrestrial lavas, the emplacement temperatures of impact melts can be much higher than the liquidus. Studies of glasses from the Ries impact structure in Germany (Hörz, 1965; El

Goresy, 1965; Grieve et al., 1977) support the assumption of superheating by several hundred degrees Celsius. There is also evidence for superheating in lunar impact melts. By examining clast digestion in lunar melt rocks, Simonds et al. (1976) suggest temperatures upwards of 1450 °C, for a liquidus of 1310°C. Thus, impact melts may be emplaced at much higher temperatures than lava flows, which typically have temperatures just above the liquidus. Due to the higher temperatures, impact melts will have lower viscosities than terrestrial lava flows, and the onset of microlite formation may be delayed until the liquidus temperatures are reached (although fine clasts may act as nucleation sites). This may only occur after the flows have travelled considerable distances. Impact melts will also include clastic material not found in terrestrial lava flows (Grieve et al., 1977).

Given these considerations, cooling an impact melt may be a much different process than cooling a lava flow, and result in different surface textures. For example, impact melt deposits may be composed of more glassy material. Evidence of glass is observed in some lunar impact melt deposits (Smrekar and Pieters, 1985; Dhingra et al., 2013). Lava flow experiments conducted with superheated lunar simulants (similar to those described in Lev et al. (2012)) coupled with thermo-rheological models are needed in order to shed light on the unusual rheology of impact melt flows and the resulting surface textures. We note that impact gardening would still affect these flows, so any blocky impact melts would have to be sufficiently thick to allow exposure of additional rough terrain under the original flow surface (Fig. 16b). We estimate that the flows would have to be more than several meters thick to survive billions of years of exposure, as lunar regolith production is estimated to be 10 cm per 100 Myr (Melosh, 1989).

Lunar impact melt flows will also experience different surface cooling conditions than terrestrial lava flows. Surface cooling is quite sensitive to the efficiency of convective cooling by the atmosphere (Keszthelyi and Denlinger, 1996), and will likely differ under vacuum conditions. Thus, cooling an impact melt flow through convection in an atmosphere may produce different surface textures than cooling an identical impact melt flow through radiation in a vacuum. Although we have yet to identify a terrestrial analogue for lunar impact melt flows, there may be analogue lava and/or impact melt flows on other planets. The lower atmospheric pressure on Mars may affect the cooling of lavas compared to the Earth, resulting in different surface textures. Indeed, many lava flows on Mars have circular polarization ratios that exceed one (Harmon et al., 2012). On the other hand, initial results suggest that impact melt deposits cooled by convection on Venus have lower circular polarization ratios than impact melt deposits cooled through radiation on the Moon (Dong and Carter, 2014). This observation supports the idea that the atmosphere (or lack thereof) could play an important role in impact melt texture. Future comparisons to lava and impact melt flows on other terrestrial planets may help to identify new analogues to lunar impact melt flows.

5. Conclusions

We compared the roughness properties of lunar impact melt flows to a variety of terrestrial lava flows, including ‘slabby’ and ‘rubbly’ transitional basaltic lava flows. The surface texture of impact melt flows is unlike that of any terrestrial lava flow yet investigated. Blocky lava flows have similar decimeter-scale radar returns to lunar impact melt flows, but tend to be rougher at the meter scale. Hawaiian pāhoehoe lava flows have similar meter scale roughness characteristics, but are much smoother at the decimeter scale. The closest analogue yet identified is a rubbly lava flow from the recent Holuhraun eruption in Iceland, although even this flow lacks the extreme values of circular polarization ratio (~0.5 vs. > 1) observed in lunar impact melt flows.

The differences between terrestrial lava flows and lunar impact melt flows may relate to (a) differences due to post-emplacment modification through impact gardening and/or erosion or (b) fundamental differences in the surface texture of the melt flows due to differences in their emplacement and/or cooling environment. Future work is needed to better understand how these unique materials were formed and altered with time. Characterizing their surface properties will be crucial for any robotic or human explorer wishing to sample these materials.

Acknowledgments

We thank the LRO, AIRSAR, and UAVSAR projects for their effort in returning the data presented here. Data from the LRO mission is made publicly available through the Planetary Data System (pds.nasa.gov). Data from the AIRSAR and UAVSAR projects were freely obtained at <http://airsar.jpl.nasa.gov/> and <http://uavsar.jpl.nasa.gov>, respectively. The fieldwork in Idaho was conducted in conjunction with the FINESSE (Field Investigations to Enable Solar System Science and Exploration) project of the Solar System Exploration Research Virtual Institute (SSERVI), led by PI J. Heldmann. Fieldwork in the Hawai'i Volcanoes National Park was conducted under Scientific Research and Collecting Permit # HAVO-2006-SCI-0003. Assistance with the dGPS surveys was provided by J. Carlin, S. Squyres, B. Caldwell, A. Bramson, L. Kestay, C. Dundas, A. Ryan, M. Sori, and A. Keske. Topographic profiles from Idaho, Hawai'i, and Iceland may be obtained from CDN (cneish@uwo.ca). CDN acknowledges support from the National Sciences and Engineering Research Council of Canada and CWH acknowledges support from the NASA Solar System Workings (SSW) Program (Grant #NNX15AL60G). We thank two anonymous reviewers for comments that helped to improve the manuscript.

References

- Bandfield, J.L., Ghent, R.R., Vasavada, A.R., Paige, D.A., Lawrence, S.J., Robinson, M.S., 2011. Lunar surface rock abundance and regolith fines temperatures derived from LRO Diviner Radiometer data. *J. Geophys. Res.* 116. doi:10.1029/2011JE003866.
- Bandfield, J.L., Hayne, P.O., Williams, J.P., Greenhagen, B.T., Paige, D.A., 2015. Lunar surface roughness derived from LRO Diviner Radiometer observations. *Icarus* 248, 357–372. doi:10.1016/j.icarus.2014.11.009.
- Braden, S.E., Stopar, J.D., Robinson, M.S., Lawrence, S.J., van der Bogert, C.H., Hiesinger, H., 2014. Evidence for basaltic volcanism on the Moon within the past 100 million years. *Nat. Geosci.* 7, 787–791. doi:10.1038/ngeo2252.
- Bray, V.J., Tornabene, L.L., Keszthelyi, L.P., McEwen, A.S., Hawke, B.R., Giguere, T.A., Katthenhorn, S.A., Garry, W.B., Rizk, B., Caudill, C.M., Gaddis, L.R., van der Bogert, C.H., 2010. New insight into lunar impact melt mobility from the LRO camera. *Geophys. Res. Lett.* 37. doi:10.1029/2010GL044666.
- Bulmer, M.H., Glaze, L.S., Anderson, S., Shockey, K.M., 2005. Distinguishing between primary and secondary emplacement events of blocky volcanic deposits using rock size distributions. *J. Geophys. Res.-Planet.* 110 (B1). doi:10.1029/2003JB002841.
- Byrnes, J.M., Crown, D.A., 2001. Relationships between pahoehoe surface units, topography, and lava tubes at Mauna Ulu, Kilauea Volcano, Hawaii. *J. Geophys. Res.* 106 (B2), 2139–2151.
- Cahill, J.T.S., Thomson, B.J., Patterson, G.W., Bussey, D.B.J., Neish, C.D., Lopez, N.R., Turner, F.S., Aldridge, T., McAdam, M., Meyer, H.M., Raney, R.K., Carter, L.M., Spudis, P.D., Hiesinger, H., Pasckert, J.H., 2014. The Miniature Radio Frequency instrument's (Mini-RF) global observations of Earth's Moon. *Icarus* 243, 173–190. <http://doi.org/10.1016/j.icarus.2014.07.018>.
- Campbell, B.A., 2002. *Radar Remote Sensing of Planetary Surfaces*. Cambridge University Press, Cambridge, U.K.
- Campbell, B.A., 2012. High circular polarization ratios in radar scattering from geologic targets. *J. Geophys. Res.* 117 (E06008). doi:10.1029/2012JE004061.
- Campbell, B.A., Shepard, M.K., 1996. Lava flow surface roughness and depolarized radar scattering. *J. Geophys. Res.* 101, 18941–18951. doi:10.1029/95JE01804.
- Campbell, B.A., Zisk, S.H., Mouginiis-Mark, P.J., 1989. A quad-pol radar scattering model for use in remote sensing of lava flow morphology. *Remote Sens. Environ.* 30, 227–237. doi:10.1016/0034-4257(89)90064-3.
- Campbell, B., Arvidson, R., Shepard, M., 1993. Radar polarization properties of volcanic and playa surfaces - applications to terrestrial remote-sensing and venus data interpretation. *J. Geophys. Res.* 98, 17099–17113.
- Campbell, B., Campbell, D., DeVries, C., 1999. Surface processes in the Venus highlands: results from analysis of Magellan and Arecibo data. *J. Geophys. Res.* 104, 1897–1916.
- Campbell, B.A., Hawke, B.R., Campbell, D.B., 2009a. Surface morphology of domes in the Marius Hills and Mons Rümker regions of the Moon from Earth-based radar data. *J. Geophys. Res.* 114. doi:10.1029/2008JE003253.
- Campbell, B.A., Hawke, B.R., Carter, L.M., Ghent, R.R., Campbell, D.B., 2009b. Rugged lava flows on the Moon revealed by Earth-based radar. *Geophys. Res. Lett.* 36, L22201–L22205. doi:10.1029/2009GL041087.
- Campbell, B.A., Carter, L.M., Campbell, D.B., Nolan, M., Chandler, J., Ghent, R.R., Hawke, B.R., Anderson, R.F., Wells, K., 2010. Earth-based 12.6 cm wavelength radar mapping of the Moon: new views of impact melt distribution and mare physical properties. *Icarus* 208, 565–573. doi:10.1016/j.icarus.2010.03.011.
- Campbell, B.A., Ray Hawke, B., Morgan, G.A., Carter, L.M., Campbell, D.B., Nolan, M., 2014. Improved discrimination of volcanic complexes, tectonic features, and regolith properties in Mare Serenitatis from Earth-based radar mapping. *J. Geophys. Res.* 119 (2), 313–330. doi:10.1002/2013JE004486.
- Carter, L.M., Neish, C.D., Bussey, D.B.J., Spudis, P.D., Patterson, G.W., Cahill, J.T., Raney, R.K., 2012. Initial observations of lunar impact melts and ejecta flows with the Mini-RF radar. *J. Geophys. Res.* 117. doi:10.1029/2011JE003911.
- Carter, L.M., Hawke, B.R., Garry, W.B., Campbell, B.A., Giguere, T.A., Bussey, D.B.J., 2013. Radar observations of lunar hollow terrain. In: *Lunar and Planetary Science Conference*, 44, p. 2146.
- Carter, L.M., Neish, C.D., Patterson, G.W., Bussey, D.B.J., Cahill, J.T.S., Nolan, M.C., Thomson, B.J., 2014. The Mini-RF Radar: polarization performance and comparison with prior radar data. In: *Lunar and Planetary Science Conference*, 45, p. 2152.
- Carter, L.M., Campbell, B.A., Neish, C.D., Nolan, M.C., Patterson, G.W., Jensen, J.R., Bussey, D.B.J., 2016. A Comparison of Radar polarimetry data of the Moon from the LRO Mini-RF instrument and Earth-based systems. *IEEE Trans. Geosci. Remote Sens.* in review.
- Cintala, M.J., Grieve, R.A.F., 1998. Scaling impact-melt and crater dimensions: Implications for the lunar cratering record. *Meteorit. Planet. Sci.* 33, 889.
- Denevi, B.W., Koeber, S.D., Robinson, M.S., Garry, W.B., Hawke, B.R., Tran, T.N., Lawrence, S.J., Keszthelyi, L.P., Barnouin, O.S., Ernst, C.M., Tornabene, L.L., 2012. Physical constraints on impact melt properties from Lunar Reconnaissance Orbiter Camera images. *Icarus* 219, 665–675. doi:10.1016/j.icarus.2012.03.020.
- Dhingra, D., Pieters, C.M., Head, J.W., Isaacson, P.J., 2013. Large mineralogically distinct impact melt feature at Copernicus crater - evidence for retention of compositional heterogeneity. *Geophys. Res. Lett.* 10. doi:10.1002/grl.50255.
- Dong, C., Carter, L.M., 2014. Analysis and comparison of physical properties and morphology of impact melt flows on Venus and the Moon. In: *American Geophysical Union, Fall Meeting 2014*, pp. P21B–3914. Abstract.
- El Goresy, A., 1965. Baddeleyite and its significance in impact glasses. *J. Geophys. Res.* 70, 3453–3456. doi:10.1029/JZ070i014p03453.
- Evans, D., Farr, T., Ford, J., Thompson, T., Werner, C., 1986. Multipolarization Radar images for geologic mapping and vegetation discrimination. *IEEE Trans. Geosci. Remote Sens.* 24, 246–257. doi:10.1109/TGRS.1986.289644, GE-24.
- Ghent, R.R., Gupta, V., Campbell, B.A., Ferguson, S.A., Brown, J.C.W., Ferguson, R.L., Carter, L.M., 2010. Generation and emplacement of fine-grained ejecta in planetary impacts. *Icarus* 209, 818–835. <http://doi.org/10.1016/j.icarus.2010.03.011>.
- Ghent, R.R., Carter, L.M., Bandfield, J.L., Tai Udovicic, C.J., Campbell, B.A., 2016. Lunar crater ejecta: physical properties revealed by radar and thermal infrared observations. *Icarus* 273, 182–195. doi:10.1016/j.icarus.2015.12.014.
- Gíslason, S.R., Stefánsson, G., Pfeffer, M., Barsotti, S., Jóhannsson, Th., Galeczka, I., Bali, E., Sigmarrsson, O., Stefánsson, A., Keller, N.S., Sigurdsson, Á., Bergsson, B., Galle, B., Jacobo, V.C., Arellano, S., Aiuppa, A., Jónasdóttir, E.B., Eiríksdóttir, E.S., Jakobsson, S., Guðfinnsson, G.H., Halldórsson, S.A., Gunnarsson, H., Haddadi, B., Jónsdóttir, I., Thorda Höskuldsson Höskuldsson, Th., Riisshuus, M., Högnadóttir, Th., Dürig, T., Pedersen, G.B.M., Höskuldsson, Á., Gudmundsson, M.T., 2015. Environmental pressure from the 2014–15 eruption of Bárðarbunga volcano, Iceland. *Geochem. Perspect. Lett.* 1, 84–93. doi:10.7185/geochemlet.1509.
- Gregg, T.K.P., Fink, J.H., 2000. A laboratory investigation into the effects of slope on lava flow morphology. *J. Volcanol. Geotherm. Res.* 96, 145–159. doi:10.1016/S0377-0273(99)00148-1.
- Grieve, R.A.F., Dence, M.R., Robertson, P.B., 1977. In: Roddy, D.J., Pepin, R.O., Merrill, R.B. (Eds.), *Cratering Processes: As Interpreted from the Occurrences of Impact Melts, in Impact and Explosion Cratering*. Pergamon Press, New York, NY, p. 791.
- Guilbaud, M.-N., Self, S., Thordarson, T., Blake, S., 2005. Morphology, surface structures, and emplacement of lavas produced by Laki, A.D. 1783–1784. *Geol. Soc. Am.* 396, 81–102. doi:10.1130/0-8137-2396-5.81, Special papers.
- Hamilton, C.W., Thordarson, T., Fagents, S.A., 2010. Explosive lava-water interactions I: architecture and emplacement chronology of volcanic rootless cone groups in the 1783–1784 Laki lava flow, Iceland. *Bull. Volcanol.* 72, 449–467. doi:10.1007/s00445-009-0330-6.
- Hamilton, C.W., 2015. Team gets firsthand look at the new Holuhraun eruption site. *Eos* 96. doi:10.1029/2015EO041197.
- Harmon, J.K., Nolan, M.C., Husmann, D.L., Campbell, B.A., 2012. Arecibo radar imagery of Mars: the major volcanic provinces. *Icarus* 220, 990–1030. doi:10.1016/j.icarus.2012.06.030.
- Hawke, B.R., Head, J.W., 1977. Impact melt in lunar crater interiors. In: Roddy, D.J., Pepin, R.O., Merrill, R.B. (Eds.), *Impact and Explosion Cratering*. Pergamon Press, New York, NY, p. 815.
- Henriksen, M.R., Manheim, M.R., Burns, K.N., Seymour, P., Speyerer, E.J., Deran, A., Boyd, A.K., Howington-Kraus, E., Rosiek, M.R., Archinal, B.A., Robinson, M.S., 2016. Extracting accurate and precise topography from LROC narrow angle camera stereo observations. *Icarus* doi:10.1016/j.icarus.2016.05.012, in press.

- Hensley, S., Wheeler, K., Sadowy, G., Miller, T., Shaffer, S., Muellerschoen, R., Jones, C., Zebker, H., Madsen, S., Rosen, P., 2005. Status of a UAVSAR designed for repeat pass interferometry for deformation measurements. In: Presented at the Microwave Symposium Digest, 2005 IEEE MTT-S International. IEEE, pp. 1453–1456. doi:10.1109/MWSYM.2005.1516963.
- Hörz, F., 1965. Untersuchungen an Riesgläsern. Beiträge zur Mineralogie und Petrographie 11, 621–661. doi:10.1007/BF01128707.
- Howard, K.A., Wilshire, H.G., 1975. Flows of impact melt at lunar craters. *J. Res. U.S. Geol. Surv.* 3, 237.
- Hughes, S.S., Smith, R.P., Hackett, W.R., Anderson, S.R., 1999. Mafic volcanism and environmental geology of the eastern Snake River Plain, Idaho. In: Hughes, S.S., Thackray, G.D. (Eds.), *Guidebook to the Geology of Eastern Idaho*. Idaho Museum of Natural History, Pocatello, Idaho, pp. 143–168.
- Hughes, S.S., Wetmore, P.H., Casper, J.L., 2004. Evolution of quaternary tholeiitic basalt eruptive centers on the eastern Snake River Plain, Idaho. In: Bonnicksen, B., White, C., McCurry, M. (Eds.), *Tectonic and Magmatic Evolution of the Snake River Plain Volcanic Province*. Idaho Geological Survey Bulletin 30, Moscow, Idaho, pp. 363–385.
- Keszthelyi, L., Denlinger, R., 1996. The initial cooling of pahoehoe flow lobes. *Bull. Volcanol.* 58, 5–18. doi:10.1007/s004450050121.
- Keszthelyi, L., Thordarson, T., McEwen, A., Haack, H., Guilbaud, M.-N., Self, S., Rossi, M.J., 2004. Icelandic analogs to Martian flood lavas. *Geochem. Geophys. Geosyst.* 5, Q11014. doi:10.1029/2004GC000758.
- Khan, S.D., Heggy, E., Fernandez, J., 2007. Mapping exposed and buried lava flows using synthetic aperture and ground-penetrating radar in Craters of the Moon lava field. *Geophysics* 72, B161–B174. doi:10.1190/1.2793298.
- Kuntz, M.A., Covington, H.R., Schorr, L.J., 1992. An overview of basaltic volcanism of the eastern Snake River Plain, Idaho. *GSA Memoirs* 179, 227–268. doi:10.1130/MEM179-p227.
- Lev, E., Spiegelman, M., Wysocki, R.J., Karson, J.A., 2012. Investigating lava flow rheology using video analysis and numerical flow models. *J. Volcanol. Geotherm. Res.* 247–248, 62–73. doi:10.1016/j.jvolgeores.2012.08.002.
- Melosh, H.J., 1989. *Impact Cratering*. Oxford University Press, Oxford, U.K.
- Morris, A.R., Anderson, F.S., Mougins-Mark, P.J., Haldemann, A.F.C., Brooks, B.A., Foster, J., 2008. Roughness of Hawaiian volcanic terrains. *J. Geophys. Res.* 113, E12007. doi:10.1029/2008JE003079.
- Neish, C.D., Madden, J., Carter, L.M., Hawke, B.R., Giguere, T., Bray, V.J., Osinski, G.R., Cahill, J.T.S., 2014. Global distribution of lunar impact melt flows. *Icarus* 239, 105–117. doi:10.1016/j.icarus.2014.05.049.
- Nord, M.E., Nord, M.E., Ainsworth, T.L., Jong-Sen, Lee, Stacy, N.J.S., 2009. Comparison of compact polarimetric synthetic aperture Radar modes. *IEEE Trans. Geosci. Remote Sens.* 47, 174–188. doi:10.1109/TGRS.2008.2000925.
- Nozette, S., Spudis, P., Bussey, B., Jensen, R., Raney, K., Winters, H., Lichtenberg, C.L., Marinelli, W., Crusan, J., Gates, M., Robinson, M., 2010. The Lunar reconnaissance orbiter Miniature Radio Frequency (Mini-RF) technology demonstration. *Space Sci. Rev.* 150, 285–302. doi:10.1007/s11214-009-9607-5.
- Osinski, G.R., Tornabene, L.L., Grieve, R.A.F., 2011. Impact ejecta emplacement on terrestrial planets. *Earth Planet. Sci. Lett.* 310, 167–181. doi:10.1016/j.epsl.2011.08.012.
- Paige, D.A., Foote, M.C., Greenhagen, B.T., Schofield, J.T., Calcutt, S., Vasavada, A.R., Preston, D.J., Taylor, F.W., Allen, C.C., Snook, K.J., Jakosky, B.M., Murray, B.C., Soderblom, L.A., Jau, B., Loring, S., Bulharowski, J., Bowles, N.E., Thomas, I.R., Sullivan, M.T., Avis, C., De Jong, E.M., Hartford, W., McCleese, D.J., 2010. The Lunar reconnaissance orbiter Diviner Lunar Radiometer experiment. *Space Sci. Rev.* 150, 125–160. doi:10.1007/s11214-009-9529-2.
- Pedersen, G.B.M., Höskuldsson, A., Riishuus, M., Jónsdóttir, I., Gudmundsson, M.T., Sigmundsson, F., Óskarsson, B.V., Dürig, T., Drouin, V.J.P.B., Gallagher, C., Askew, R., Moreland, W.M., Dumont, S., Davies, A., Keszthelyi, L., Hamilton, C.W., Þórdarson, Þ., 2015. Nornahraun lava morphology and emplacement: a new terrestrial analogue for planetary lava flows. In: *Lunar and Planetary Science Conference*, 46, p. 1845.
- Peterson, D.W., Swanson, D.A., 1974. Observed formation of lava tubes during 1970–1971 at Kilauea Volcano, Hawaii. *Stud. Speleol.* 2, 209–222.
- Raney, R.K., 2006. Dual-polarized SAR and Stokes parameters. *IEEE Geosci. Remote Sens. Lett.* 3, 317–319. doi:10.1109/LGRS.2006.871746.
- Raney, R.K., Cahill, J.T.S., Patterson, G.W., Bussey, D.B.J., 2012. The m-chi decomposition of hybrid dual-polarimetric radar data with application to lunar craters. *J. Geophys. Res.* 117. doi:10.1029/2011JE003986.
- Robinson, M.S.22 colleagues, 2010. Lunar Reconnaissance Orbiter Camera (LROC) instrument overview. *Space Sci. Rev.* 150, 81–124. doi:10.1007/s11214-010-9634-2.
- Rowland, S.K., Walker, G.P.L., 1987. Toothpaste lava: characteristics and origin of a lava structural type transitional between pahoehoe and a'a. *Bull. Volcanol.* 49, 631–641.
- Shepard, M.K., Campbell, B.A., Bulmer, M.H., Farr, T.G., Gaddis, L.R., Plaut, J.J., 2001. The roughness of natural terrain: a planetary and remote sensing perspective. *J. Geophys. Res.* 106, 32777–32795.
- Simonds, C.H., Warner, J.L., Phinney, W.C., 1976. Thermal regimes in cratered terrain with emphasis on the role of impact melt. *Am. Mineral.* 61, 569–577.
- Smrekar, S., Pieters, C.M., 1985. Near-infrared spectroscopy of probable impact melt from three large lunar highland craters. *Icarus* 63, 442–452. doi:10.1016/0019-1035(85)90056-9.
- Stopar, J.D., Hawke, B.R., Robinson, M.S., Denevi, B.W., Giguere, T.A., Koeber, S.D., 2014. Occurrence and mechanisms of impact melt emplacement at small lunar craters. *Icarus* 243, 337–357. doi:10.1016/j.icarus.2014.08.011.
- Swanson, D.A., Duffield, W.A., Jackson, D.B., Peterson, D.W., 1979. Chronological narrative of the 1969–1971 Mauna Ulu eruption of Kilauea Volcano, Hawaii, 1056, pp. 1–55. U. S. Geological Survey Professional Paper.
- Tilling, R.I., Christiansen, R.L., Duffield, W.A., Endo, E.T., Holcomb, R.T., Koyanagi, R.Y., Peterson, D.W., Unger, J.D., 1987. The 1972–1974 Mauna Ulu eruption, Kilauea Volcano: an example of quasi-steady-state magma transfer. In: Decker, R.W., Wright, T.L., Stauffer, P.H. (Eds.), *Volcanism in Hawaii*, pp. 405–469. U. S. Geological Survey Professional Paper, I350.
- Turcotte, D.L., 1997. *Fractals and Chaos in Geology and Geophysics*, (second ed.) Cambridge University Press, Cambridge, U.K.
- Walker, G.P.L., 1991. Structure and origin by injection of, lava under surface crust, of tumuli, “lava rises”, “lava-rise pits”, and “lava-inflation clefts”. *Hawai'i Bull. Volcanol.* 53, 546–558.
- Zanetti, M., Neish, C., Choe, B.-H., Heldmann, J.L., 2016. Mapping fresh lava flows with multi-wavelength radar imagery in support of planetary analogue studies. *Icarus* 47, p. 2429.
- Zebker, H.A., Lou, Y., 1990. Phase calibration of imaging radar polarimeter Stokes matrices. *IEEE Trans. Geosci. Remote Sens.* 28 (2), 246–252. doi:10.1109/36.46704.